Master Thesis
Physics

Submitted to the III. Institute of Physics B at the
Faculty for Mathematics, Computer Science and Natural Science

RWTH AACHEN UNIVERSITY

Investigation of the Spin Coherence Time for measuring the Electric Dipole Moment of Protons in the COSY Cooler Synchrotron

---

Daoning Gu

1. Examiner: Prof. Dr. Andreas Lehrach
2. Examiner: Prof. Dr. Jörg Pretz

Aachen, October 2022

Abstract

Assuming that the CPT theorem holds, an Electric Dipole Moment (EDM) is also a source of CP violation, which is needed to explain the matter-antimatter asymmetry. Measuring an EDM at a higher value than the SM prediction would therefore provide an additional CP violation and would be a strong indication for physics beyond the SM.
The JEDI-Collaboration (Jülich Electric Dipole moment Investigations) is planning to use the storage rings COSY (COoler SYnchrotron) for high precision proton beam EDM experiments. In order to achieve a sufficient statistical sensitivity, it is necessary to have a long Spin Coherence Time (SCT).
In this thesis, spin tracking simulations were performed with the software library Bmad to investigate the sextupole contributions. By using the FFT/NAFF algorithm that reduces the modulation of synchrotron oscillations, the spin tune can be precisely calculated. Simulations were performed to verify the linear relationship between some important parameters of the proton beam and the inverse of the SCT. Based on the assumption of a linear system of equations, the optimal setup for the three families of sextupoles in an ideal lattice is found via spin tracking simulations. This made it possible to achieve a long SCT for proton beams.

Contents

Acronyms

COSY COoler SYnchrotron

EDM Electric Dipole Moment

MDM Magnetic Dipole Moment

JEDI Jülich Electric Dipole moment Investigations

JULIC Jülich Light Ion Cyclotron

SM Standard Model of particle physics

SCT Spin Coherence Time

RF Radio Frequency

APA Average phase advance

FFT fast Fourier transform

NAFF Numerical Analysis of Fundamental Frequencies

List of Figures

List of Tables

1. Introduction

The inability of the Standard Model (SM) to explain the matter-antimatter asymmetry in the universe is one of the most challenging problems in modern physics. The Electric Dipole Moment (EDM) of a subatomic particle is predicted by the SM and provides simultaneous violation of parity (P) and time reversal (T). EDM is a source of CP violations when the CPT theorem is assumed to be valid. This is the key to explaining the problem of matter-antimatter asymmetry. Therefore, measuring the EDM at a value higher than that predicted by the SM would indicate an additional CP violation and would be evidence of physics beyond the SM.

Optimization of the Spin Coherence Time (SCT) plays a central role in storage ring EDM experiments, since a long SCT is required to achieve the statistical sensitivity for an EDM measurement. After a sufficient long SCT was achieved for deuteron beams, the JEDI-Collaboration (Jülich Electric Dipole moment Investigations) in Jülich is preparing a similar measurement for the SCT for protons at the storage ring COSY (COoler SYnchrotron).[22]
Many parameters indicate that for proton beams, the optimization procedure to realize long SCT is more difficult than for deuteron beams. On the one hand, the anomalous gyromagnetic g-factor G of the proton is more than an order of magnitude larger than that of the deuteron. On the other hand, the intrinsic spin resonances are much higher in number and intensity. As shown in previous simulations, this leads to a significant reduction in the SCT, which must be very finely optimised by sextupole corrections.[23]

The task of this thesis is to perform spin tracking simulations for investigating the sextupole's contributions. Firstly the model of COSY needs to be implemented into the software library Bmad. Next the dependences of important beam parameters such as the emittance and the momentum spread on the SCT should be checked. Furthermore, an optimal sextupole setting needs to be found to achieve the longest SCT. In this thesis, the COSY lattice used is the ideal model without misalignment.

This thesis is structured as follows: Chapter 2 provides the scientific motivation and the theoretical background of the EDM measurements. The basic concepts and equations of beam dynamics and spin dynamics are described in chapters 3 and 4. In chapter 5 an introduction to the accelerator facility COSY is given, a description of how the model is implemented in the simulation software is explained, and different algorithms for calculating spin tune are also discussed. In Chapter 6, the beam parameters and particle distribution used in the simulations are investigated, the

linear dependence of emittance and momentum spread on SCT is verified, and the scan studies of chromaticity are shown. The methods used to optimise the spin coherence time and the results obtained for a long SCT are presented in Chapter 7. Chapter 8 summarises the results in this thesis and gives an outlook.

2. Scientific motivation

2.1. Matter antimatter asymmetry

Why there is more matter than antimatter after the big bang? It is a big question in modern physics. This excess of matter can be expressed by the baryon-to-photon density ratio, also known as baryon asymmetry:

$$\eta = \frac{n_b - n_{\bar{b}}}{n_\gamma} = (6.129 \pm 0.039) \times 10^{-10}, \tag{2.1}$$

where η refers to the baryon asymmetry, n_b, $n_{\bar{b}}$ and n_γ are the baryon, antibaryon and photon densities respectively.[28] However, the current Standard Model of Cosmology theory only predict 10^{-18} for the same number.[12] So there is a big discrepancy. One possible explanation is that the antimatter was annihilated in asymmetric processes during the evolution of the Universe, and this requires the fulfilment of three conditions proposed by Sakharov.[5]

- **Baryon number violation:** There exists interactions that violate the baryon number, since the net baryon number of the universe must vary with time.

- ***C* and *CP* violation:** Only if C and CP are asymmetric will the baryon production rate not be equal to the anti-baryon production rate, so that a net baryon number can be generated.

- **Departure from thermal equilibrium:** The process that violates the baryon number must be out of thermal equilibrium. Otherwise, the CPT symmetry at equilibrium would prevent the baryon number from being generated.

2.2. Electric dipole moment

The EDM originates from the permanent separation of positive and negative charges within the particle. In particle physics, the EDM $\vec{d}$ and Magnetic Dipole Moment (MDM) $\vec{\mu}$ are fundamental properties of particles. By definition, dipole moments must be either parallel or antiparallel with respect to the spin direction. The non-relativistic Hamiltonian of a corresponding particle in electromagnetic fields can be written as:

$$H = -\vec{\mu} \cdot \vec{B} - \vec{d} \cdot \vec{E}, \tag{2.2}$$

where $\vec{E}$ is the electric field and $\vec{B}$ is the magnetic field.
Under the parity P transformation, only the electric field $\vec{E}$ inverts its sign, while the magnetic field $\vec{B}$ and spin (i.e. $\vec{\mu}$ and $\vec{d}$) remain unchanged. In the case of a time reversal T transformation, the magnetic field $\vec{B}$ and the spin vector flip their signs while the electric field $\vec{E}$ does not change. [23], Above transformations are illustrated by the Equations 2.3 and Figure 2.1.

$$\begin{aligned} P &: H = -\vec{\mu} \cdot \vec{B} + \vec{d} \cdot \vec{E}, \\ T &: H = -\vec{\mu} \cdot \vec{B} + \vec{d} \cdot \vec{E}. \end{aligned} \tag{2.3}$$

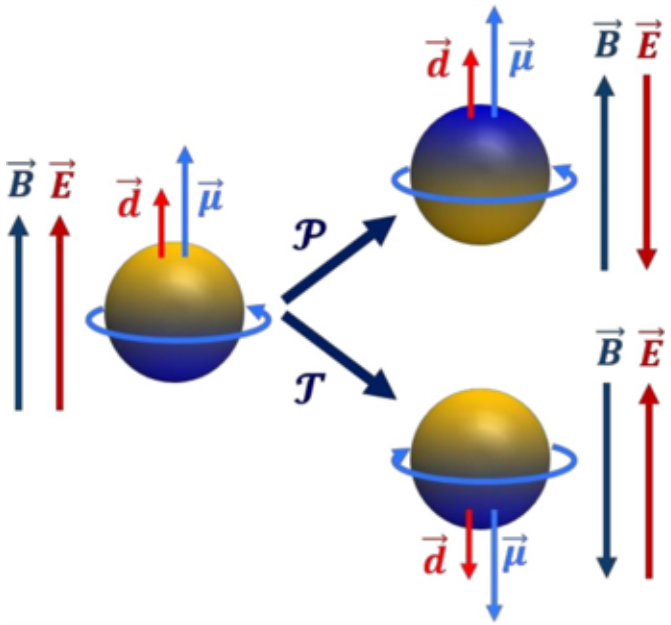

Figure 2.1.: The schematic shows a particle undergoing parity and time-reversal transformations in an electromagnetic field. The EDM term violates the P and T symmetries, according to the CPT theorem also violates the CP symmetry. Taken from [32]

Assuming the CPT theorem holds, since the EDM term $\vec{d} \cdot \vec{E}$ breaks P and T symmetry, therefore it is also a source of CP violation. The Standard Model predicts the nuclear EDMs are of order 10^{-31} to 10^{-33} e cm.[25] Measurements of higher values of the EDM will be interpreted as a sign of new physics beyond the Standard Model.

3. Beam dynamics in storage rings

The proposed EDM measurement of charged particles can be realized at a storage ring. In this chapter a brief introduction to the basic concepts and equations of beam dynamics will be given. The brief descriptions presented here are mainly taken from [11], [21] and [31].

3.1. Charged particles motion

A beam describes an ensemble of charged particles in very similar state of motion. These particles have almost the same momentum and are spatially concentrated. In a storage ring, the charged particles travel on a circular orbit. The angular divergences as well as the momentum deviation of the individual particles inside the beam are a potential cause of their loss on this orbit. In order to correct the trajectory of the particles, one needs to guide them back to the reference orbit. In general, this is achieved by electromagnetic fields applied to the charged particles:[11]

$$\vec{F} = q \cdot (\vec{E} + \vec{v} \times \vec{B}) \tag{3.1}$$

Equation 3.1 shows the Lorentz force where a particle of charge q and velocity $\vec{v}$ experiences a force $\vec{F}$ due to an electric field $\vec{E}$ and a magnetic field $\vec{B}$.

3.2. Coordinate system

In order to observe and describe the motion of a particle, a coordinate system needs to be established. In this thesis a co-moving coordinate system (shown in Figure 3.1) is used, where the origin of the coordinates is always fixed on the reference particle. Therefore, the origin of the coordinates follows the orbit of the reference particle. This orbit is called the ideal or reference orbit and generally consists of straight and curved segments. Usually, one assume that the ideal orbit lies on the same horizontal plane, which is called the orbital plane.
The three axes of the coordinate system are orthogonal to each other. In this thesis, the s-axis is always along the ideal orbit, pointing in the moving direction of the reference particle. The x-axis is in the plane of the storage ring, perpendicular to the s-axis, pointing out of the ring. The y-axis is perpendicular to the orbital plane and is positive above. With this coordinate system, the position of an arbitrary particle at any given moment can be marked by the three coordinate variables x, y and s. Additional information is provided by the three components of its momentum, representing the instantaneous rate of change of each of the three position variables. One can assume that the coordinate system is only rotated around the y-axis. When rotated by the angle φ, the coordinate basis vectors from point A to point B are

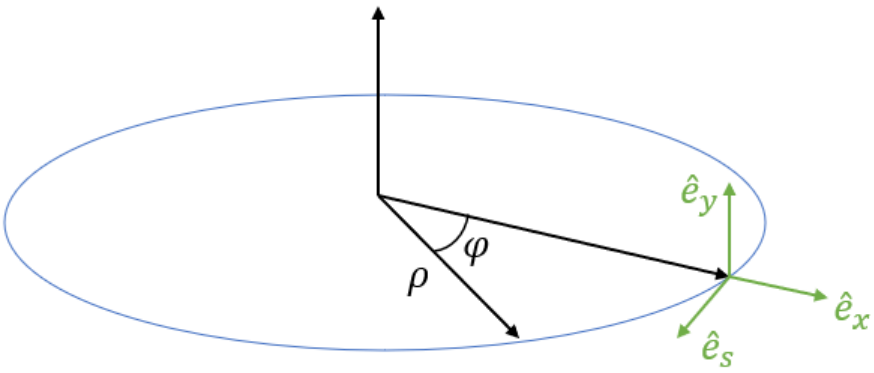

Figure 3.1.: Co-moving Cartesian coordinate system to illustrate the beam motion relative to the reference particle. $\hat{e}_s$, $\hat{e}_x$ and $\hat{e}_y$ are coordinate base vectors at one point, respectively. φ refers to the angle between the particle and the reference particle. ρ is the radius of curvature of the trajectory. Inspired by [11].

transformed as follows [11]:

$$\begin{aligned} \hat{e}_{x,B} &= cos\varphi\hat{e}_{x,A} + sin\varphi\hat{e}_{s,A} \\ \hat{e}_{y,B} &= \hat{e}_{y,A} \\ \hat{e}_{s,B} &= -sin\varphi\hat{e}_{x,A} + cos\varphi\hat{e}_{s,A} \end{aligned} \tag{3.2}$$

The relationship between arc length ds and the radius of curvature of the trajectory ρ is $ds = \rho\varphi$. Then one can calculate the time derivatives of the coordinate basis vectors as:

$$\begin{aligned} \dot{\hat{e}}_x &= \frac{\mathrm{d}\hat{e}_x}{\mathrm{d}\varphi}\frac{\mathrm{d}\varphi}{\mathrm{d}t} = \frac{\dot{s}}{\rho}\hat{e}_s \\ \dot{\hat{e}}_y &= \frac{\mathrm{d}\hat{e}_y}{\mathrm{d}\varphi}\frac{\mathrm{d}\varphi}{\mathrm{d}t} = 0 \\ \dot{\hat{e}}_s &= \frac{\mathrm{d}\hat{e}_s}{\mathrm{d}\varphi}\frac{\mathrm{d}\varphi}{\mathrm{d}t} = -\frac{\dot{s}}{\rho}\hat{e}_x \end{aligned} \tag{3.3}$$

3.2.1. Field expansion

When a particle is moving on a circular orbit, the Lorentz force provides the centripetal force if there is only a transverse magnetic field. This results in the following relation [11]:

$$\frac{1}{\rho(x,y,s)} = \frac{q}{p}B_y(x,y,s). \tag{3.4}$$

In Equation 3.4 the quantity p is the particle's momentum whereas ρ is the radius of the orbit.

Considering that the radius of curvature of the particle trajectory is much larger than the dimension of the beam, one can perform a Taylor expansion of the magnetic field along the vicinity of the ideal orbit [11]:

$$\begin{array}{llll} \frac{q}{p}B_y(x) & = \frac{q}{p}B_y(0) & +\frac{q}{p}\frac{\partial B_y}{\partial x}x & +\frac{1}{2!}\frac{q}{p}\frac{\partial^2 B_y}{\partial x^2}x^2 \quad +... \\ & = \frac{1}{\rho} & +kx & +\frac{1}{2!}mx^2 \quad +... \\ & \textit{Dipole} & \textit{Quadrupole} & \textit{Sextupole} \quad ... \\ & \textit{Bending} & \textit{Focusing} & \textit{Correction} \quad ... \end{array} \tag{3.5}$$

Equation 3.5 displays that the effects of the dipole term is beam steering, the quadrupole term is beam focusing and the sextupole term is chromaticity correcting. Higher multipoles occur due to field errors or field compensation. The linear beam optics consist of only the two lowest multipoles terms, namely the dipole term and quadrupole term.

3.3. Transverse motion

In this section, the equations of transverse motion will be discussed. For linear beam optics, the bending dipoles keep the particle's trajectory on a closed orbit, while the quadrupoles keep the particle motion stable through their transverse focusing and defocusing.

3.3.1. Hill's differential equations

Assuming that only dipole and quadrupole fields exist, one can use $x(s)$ and $y(s)$ to denote the horizontal and vertical displacement of the particle from the reference orbit, respectively. The transverse motion equations of particles in periodic fields are described by the Hill's differential equations [11]:

$$\begin{aligned} x''(s) + \left(\frac{1}{\rho^2(s)} - k(s)\right)x(s) &= \frac{1}{\rho(s)}\frac{\Delta p}{p} \\ y''(s) + k(s)y(s) &= 0 \end{aligned} \tag{3.6}$$

where momentum deviation Δp is very small compared to the particle's reference momentum p. The bending radius in the dipole field $\rho(s)$ and the quadrupole strength $k(s)$ are functions of the s-coordinate on a closed orbit, one period is defined as the circumference of the circular accelerator C_0. Since a quadrupole magnet is always focused in one plane and defocused in the other plane, in this thesis, we choose the negative sign of k as focusing and vice versa.

3.3.2. Betatron oscillation and betatron tune

Consider the case without momentum deviation $\frac{\Delta p}{p} = 0$ and a negligible weak focusing contribution $\frac{1}{\rho(s)} = 0$. The Hill's differential quations (3.6) can be rewritten as:

$$\begin{aligned} x''(s) - k(s)x(s) &= 0 \\ y''(s) + k(s)y(s) &= 0 \end{aligned} \tag{3.7}$$

As the two equations are similar in structure, only the horizontal direction x is discussed. The oscillation of a particle around a reference orbit, so called the betatron oscillation, is described by the function $x(s)$. One can make the following ansatz for the solution of the equations above:

$$x(s) = Au(s)\cos\left(\Psi(s) + \phi\right) \tag{3.8}$$

where A denotes the constant amplitude factor of the oscillation, $\Psi(s)$ the phase advance and ϕ the initial phase.
The emittance ε is a constant parameter throughout the whole beam transport system. Introducing the amplitude beta function $\beta(s) \equiv u^2(s)$, then Equation 3.8 can be expressed as:

$$x(s) = \sqrt{\varepsilon}\sqrt{\beta(s)}\cos\left(\Psi(s) + \phi\right) \tag{3.9}$$

with

$$\Psi(s) = \int_0^s \frac{d\sigma}{\beta(\sigma)}. \tag{3.10}$$

The betatron tune of the accelerator is defined as the number of oscillations per revolution [30]:

$$Q_{x,y} = \frac{\Delta\Psi}{2\pi} = \frac{1}{2\pi}\oint \frac{ds}{\beta(s)} \tag{3.11}$$

where x, y denote respectively the horizontal and vertical directions, $\Delta\Psi$ is the phase advance for a full turn.

3.3.3. Phase space ellipse

In simulations and experiments, it is often difficult to calculate the trajectory for every single particle. For a better description of the whole particle beam's motion, one can use the phase space ellipse to observe their dynamics.[21] In a two-dimensional phase space, the coordinates are the position x and the angle x' in the horizontal direction. The derivative of Hill's equation solution can be expressed as:

$$x'(s) = -\frac{\sqrt{\varepsilon}}{\sqrt{\beta(s)}}\left[\alpha(s)\cos\left(\Psi(s) + \phi\right) + \sin\left(\Psi(s) + \phi\right)\right] \tag{3.12}$$

with

$$\alpha(s) \equiv -\frac{\beta'(s)}{2}. \tag{3.13}$$

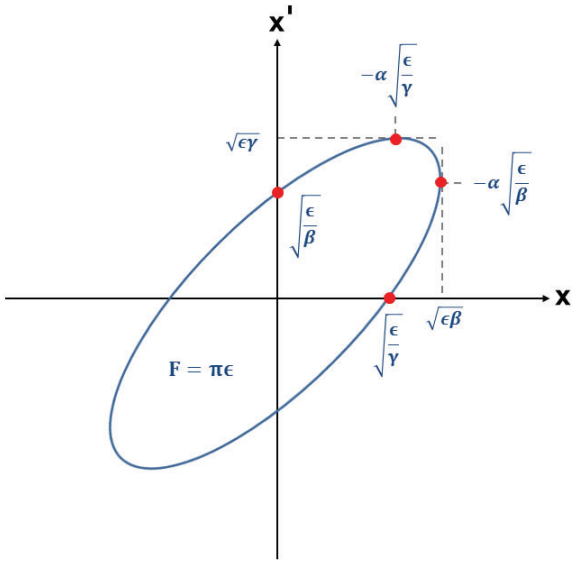

Figure 3.2.: The invariant phase space ellipse for horizontal plane at a fixed position s. The extreme values and zero crossings are Courant–Snyder (Twiss) parameters. Adapted from [21].

One can define a parameter:

$$\gamma(s) \equiv \frac{1+\alpha^2(s)}{\beta(s)} \tag{3.14}$$

then Equation (3.12) can be expressed in the form [11]:

$$\gamma(s)x^2(s) + 2\alpha(s)x(s)x'(s) + \beta(s)x'^2(s) = \varepsilon. \tag{3.15}$$

This equation describes an ellipse (see Figure 3.2) in the $(x - x')$ horizontal plane, α, β and γ are called Courant–Snyder (Twiss) parameters. The area of the ellipse is $F = \pi\varepsilon$. According to Liouville's theorem, the volume of the phase space stays constant when the beam in the accelerator is only affected by conservative forces. The shape of the phase space ellipse changes but its area remains constant as the particle travels around the accelerator.
Since the two directions in the transverse plane are uncoupled, the above discussion also applies to the vertical plane.

3.3.4. Beam emittance

For a single particle, the amplitude of its betatron oscillation in a magnetic field structure can be defined as envelope $E(s) = \sqrt{\varepsilon\beta(s)}$. One can see that the emittance ε is a constant value, while the betatron function $\beta(s)$ is position dependent especially with regard to focusing/defocusing magnets. This can be used to control the beam size at special locations.[21]

For a beam of many particles, one need a definition for the average beam emittance. Here one can assume that the distribution of the particle beam in the transverse phase space to be a Gaussian distribution:

$$\rho(x,y) = \frac{Ne}{2\pi\sigma_x\sigma_y}\exp\left(-\frac{x^2}{2\sigma_x^2} - \frac{y^2}{2\sigma_y^2}\right) \tag{3.16}$$

where N is the number of particles, σ_x and σ_y are the horizontal and vertical standard deviations of the particle distribution.
The definition of emittance ε_{STD} for the entire beam is [11]:

$$\varepsilon_{STD} = \frac{\sigma^2(s)}{\beta(s)}. \tag{3.17}$$

3.3.5. Dispersion

In the previous sections, only the homogenous solution of hills differential equations was discussed, as the momentum deviation was neglected. In a real accelerator, the particle beam is usually consisted of many off-momentum particles. Assuming that only the dipole field exists and the bending radius is ρ, then Equation (3.6) can be expressed as:

$$x'' + \frac{1}{\rho^2}x = \frac{1}{\rho}\frac{\Delta p}{p}. \tag{3.18}$$

When $\Delta p/p = 1$, the above Equation 3.18 defines the dispersion equation $D(s)$ [11]

$$D''(s) + \frac{1}{\rho^2}D(s) = \frac{1}{\rho}. \tag{3.19}$$

The complete equation solution $x_g(s)$ includes the general solution $x(s)$ of the associated homogeneous differential equation and the particular solution $x_D(s)$ of the non-homogeneous term:

$$x_g(s) = x(s) + x_D(s) = x(s) + D(s)\frac{\Delta p}{p} \tag{3.20}$$

where $x(s)$ describes the betatron oscillation and $x_D(s)$ is the offset due to a relative momentum deviation $\Delta p/p = 1$. [11]

3.3.6. Chromaticity and its compensation

For the particles with momentum deviations, similarly to the dispersion, the quadrupole field acts differently on each particle. Assuming that Δp is very small, a particle with momentum $p = p_0 + \Delta p$ will experience a modified quadrupole field [11]

$$k(p) = -\frac{q}{p}g = -\frac{q}{p_0 + \Delta p}g \approx -\frac{q}{p_0}(1 - \frac{\Delta p}{p_0})g = k_0 - \Delta k. \tag{3.21}$$

One can write the contribution of the momentum deviation effect to the quadruple error Δk as:

$$\Delta k = \frac{\Delta p}{p} k_0. \tag{3.22}$$

The quadrupole error leads to a betatron tune shift dQ:

$$dQ = \frac{\Delta p}{p} \frac{1}{4\pi} k_0 \beta(s) ds. \tag{3.23}$$

Therefore, one can define a dimensionless quantity natural chromaticity ξ via:

$$\xi \equiv \frac{\Delta Q}{\Delta p/p} = \frac{1}{4\pi} \oint k(s)\beta(s) ds. \tag{3.24}$$

It represents the total tune shift integrated along all the accelerator's quadrupoles. Since the optical function $\beta(s)$ in a focusing magnet is always larger than that in a defocusing magnet in a ring with strong focusing lattice, the natural chromaticity caused only by the quadrupole fields is always negative. [30]
The chromaticity effect caused by momentum deviations leads to tune shifts, which may eventually cause damaging resonances. In order to achieve stable operation, sextupole magnets are used in the accelerator to compensate for chromaticity. The sextupole's focusing strength is position-dependent:

$$\frac{q}{p} \vec{B}_{sext} = mxy\hat{e}_x + \frac{1}{2} m(x^2 - y^2)\hat{e}_y, \tag{3.25}$$

then given the following focusing strength k depending on dispersion D in x- and y-axes respectively [30]

$$\begin{aligned} k_x &= \frac{q}{p} \frac{\partial B_y}{\partial x} = mx = mD \frac{\Delta p}{p} \\ k_y &= \frac{q}{p} \frac{\partial B_x}{\partial y} = mx = mD \frac{\Delta p}{p}. \end{aligned} \tag{3.26}$$

Figure 3.3 is a demonstration of how a sextupole is operating. One placed the sextupole magnet after the quadrupole magnet. When a reference particle without momentum deviation $\Delta p/p = 0$ passes through, it travels in the reference orbit. since the centre of a sextupole is field-free, so the sextupole doesn't have any effect on it. For a particle with momentum deviation $\Delta p/p \neq 0$, its orbit deviates from the nominal orbit by a horizontal offset of x due to the dispersion D. This leads to an additional quadrupole strength of the sextupole

$$k_{sext} = mx = mD \frac{\Delta p}{p} \tag{3.27}$$

where m is the sextupole strength. [11]
Adding the contribution of all sextupoles, then obtain the total chromaticity

$$\xi_{tot} = \frac{1}{4\pi} \oint [m(s)D(s) + k(s)]\beta(s) ds. \tag{3.28}$$

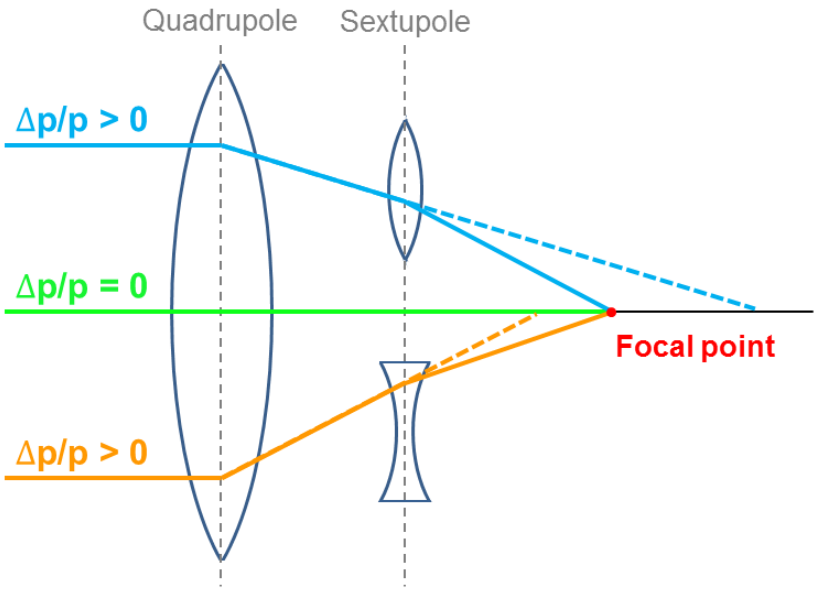

Figure 3.3.: The correcting sextupole magnet is placed to compensate the chromaticity. In regions where the dispersion is not zero, the offset particles are not passing through the magnet at the centre. The sextupole magnet produces quadrupole fields to correct for the chromaticities depending on the position of the particle. Adapted from [11].

3.4. Longitudinal motion

The previous sections are all about the transverse motion of particles in the accelerator. This section describes the longitudinal motion affected by the cavity. The cavity generates a longitudinally oscillating electric field that changes the particle's energy as it passes through the cavity. In order to keep the particle beam in a phase that is relatively stable with respect to the reference phase of the cavity, one need to adopt the method of phase focusing.

3.4.1. Momentum compaction

Consider an off-momentum particle travelling in a circular accelerator, where the bending magnet will cause the particle's trajectory to deviate from the ideal orbit. The total path length of this off-momentum particle will differ from the reference particle's path length and can be described by:

$$L = L_0 + \Delta L = \oint r d\varphi = \oint \frac{\rho + x_D}{\rho} = \oint ds + \frac{\Delta p}{p} \oint \frac{D(s)}{\rho(s)} ds \tag{3.29}$$

where L_0 stands for the path length of the reference particle.
Then one can obtain the path length change due to momentum deviation:

$$\Delta L = \frac{\Delta p}{p} \oint \frac{D(s)}{\rho(s)} ds. \tag{3.30}$$

The momentum compaction factor α, defined as the ratio of the relative change in path length $\Delta L/L_0$ to the relative difference in momentum $\Delta p/p$ for a circular accelerator, is given by [11]:

$$\alpha = \frac{\Delta L/L_0}{\Delta p/p} = \frac{1}{L_0} \oint \frac{D(s)}{\rho(s)} ds. \tag{3.31}$$

3.4.2. Phase focusing

According to the definition, the revolution time is the path length divided by the particle's velocity $T = L/v$. Using the momentum compaction factor α, the relative time difference can be derived as [11]:

$$\frac{\Delta T}{T_0} = \frac{\Delta L}{L_0} - \frac{\Delta v}{v_0} = (\alpha - \frac{1}{\gamma^2}) \frac{\Delta p}{p_0}. \tag{3.32}$$

Introducing the slip factor η:

$$\eta = \alpha - \frac{1}{\gamma_{tr}^2}, \tag{3.33}$$

where the γ_{tr} is the transition energy when η is zero. Its value is only dependent on the momentum compaction factor α:

$$\gamma_{tr} = \frac{1}{\sqrt{\alpha}}. \tag{3.34}$$

For a non-relativistic particle with the energy less than γ_{tr}, the orbital length does not change much and the change in velocity dominates the relative time difference (Equation 3.32). Above the transition energy, especially for ultra relativistic particles, the velocity of the particle is almost constant and the orbital length dominates.

Figure 3.4 shows that for relativistic particles, phase focusing is happened on the falling flank. One can define a synchronous particle, which always arrives at the cavity when the field is at the same phase. When the phase of the cavity φ_s is set to π, a synchronous particle does not gain or lose energy while passing through the RF cavity. When a particle has less momentum than the synchronous particle $\Delta p/p < 0$, it travels on a shorter trajectory than the nominal trajectory. Thus it will reach the cavity earlier with a smaller phase, which means it will gain more energy to catch up with the reference particle. And vice versa when a particle's momentum is greater than that of the synchronous particle.
In a real accelerator, particles always have a certain energy spread. The particles clump together through the cavity to form the bunches. Inside a bunch, offset particles perform synchrotron oscillations around the reference particle.[11]

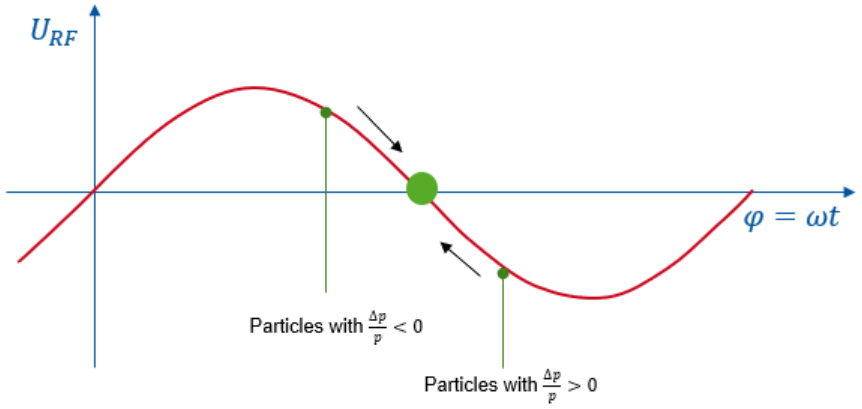

Figure 3.4.: Phase focussing of relativistic particles. The cavity is working on the bunching mode, $\varphi_s = \pi$. The horizontal coordinate is the phase of the particle. Particles with momentum deviations oscillate around the reference orbit due to phase differences.

4. Spin dynamics in storage rings

Spin motion in accelerators is often viewed as the fourth dimension of particle motion. When one studies spin dynamics, one has to consider the details of the beam dynamics carefully because of the close connection between spin motion and orbital motion. The content of this section is mainly taken from [33], [23] and [16].

4.1. Polarization

4.1.1. Spin-1/2 particles

The state of a spin -1/2 particle can be expressed by its wave function:

$$|\Psi\rangle = a\left|\chi_{+1/2}\right\rangle + b\left|\chi_{-1/2}\right\rangle \equiv a\,|\uparrow\rangle + b\,|\downarrow\rangle = a\begin{pmatrix}1\\0\end{pmatrix} + b\begin{pmatrix}0\\1\end{pmatrix} \tag{4.1}$$

where $|\uparrow\rangle$ and $|\downarrow\rangle$ represent the corresponding two spin states $m = \pm\frac{1}{2}$, respectively. [16]

Its density matrix is:

$$\rho = |\Psi\rangle\langle\Psi| = \begin{pmatrix}|a|^2 & ab^*\\ ba^* & |b|^2\end{pmatrix} \tag{4.2}$$

with $|a|^2 + |b|^2 = 1$.

Spin polarization $\vec{P}$ is defined as the expectation value of the spin operators $\vec{S}$:

$$\vec{P} = \frac{1}{N}\sum_{i=1}^{N}\vec{S}_i. \tag{4.3}$$

For a beam that contains N^+ quantization states of $+1/2$ particles and N^- quantization states of -1/2 particles, one can then introduce the definition of the vector polarization as [16]:

$$P_V = \frac{N^+ - N^-}{N^+ + N^-}. \tag{4.4}$$

4.1.2. Spin-1 particles

Similar to spin -1/2 particle, the three spin states of the spin -1 particle particle are represented by $|1\rangle$, $|0\rangle$, and $|-1\rangle$, respectively. Then its wave function can be expressed

as:

$$|\Psi\rangle = a\,|\chi_1\rangle + b\,|\chi_0\rangle + c\,|\chi_{-1}\rangle \equiv a\,|1\rangle + b\,|0\rangle + c\,|-1\rangle = \begin{pmatrix} a \\ b \\ c \end{pmatrix} \tag{4.5}$$

and [16]

$$\rho = \begin{pmatrix} |a|^2 & ab^* & ac^* \\ ba^* & |b|^2 & bc^* \\ ca^* & cb^* & |c|^2 \end{pmatrix}. \tag{4.6}$$

For a beam that contains N^+ quantization states of +1 particles, N^- quantization states of -1/2 particles and N^0 quantization states of 0 particles, the vector polarization P_V and tensor polarization P_T along the quantization axis are [16]:

$$P_V = \frac{N^+ - N^-}{N^+ + N^0 + N^-} \tag{4.7}$$

$$P_T = \frac{N^+ + N^- - 2N^0}{N^+ + N^0 + N^-} \tag{4.8}$$

4.2. The Thomas-BMT equation

In a circular accelerator, the formula describing the precession motion of a particle is called the Thomas-Bargmann-Telegdi-Michel (Thomas-BMT) equation [1][2]. The special feature of this equation is that it uses a mixture of two different reference frames. The electromagnetic field seen by the particle is transformed into the laboratory frame, while the particle's spin is in the particle's rest frame. Usually one only need to consider the Magnetic Dipole Moment (MDM) effect. A more general expression is given here, which also includes the contribution of the Electric Dipole Moment (EDM) [18]:

$$\frac{\mathrm{d}\vec{S}}{\mathrm{d}t} = \vec{\Omega}_{MDM} \times \vec{S} + \vec{\Omega}_{EDM} \times \vec{S}, \tag{4.9}$$

$$\vec{\Omega}_{MDM} = -\frac{q}{m}\left[\left(G + \frac{1}{\gamma}\right)\vec{B} - \frac{G\gamma}{\gamma+1}\left(\vec{\beta}\cdot\vec{B}\right)\vec{\beta} - \left(G + \frac{1}{\gamma+1}\right)\vec{\beta}\times\frac{\vec{E}}{c}\right], \tag{4.10}$$

$$\vec{\Omega}_{EDM} = -\frac{q}{mc}\frac{\eta_{EDM}}{2}\left[\vec{E} - \frac{\gamma}{\gamma+1}\left(\vec{\beta}\cdot\vec{E}\right)\vec{\beta} + c\vec{\beta}\times\vec{B}\right] \tag{4.11}$$

with the anomalous magnetic moment of a particle $G = \frac{g-2}{2}$.
Since the field can be divided into parallel and perpendicular components along the direction of particle's motion, one can write the total MDM terms separately as: [18]

$$\begin{aligned}\vec{\Omega}_{MDM} &= \vec{\Omega}_{B\perp} + \vec{\Omega}_{B\parallel} + \vec{\Omega}_{E\perp} \\ &= -\frac{q}{\gamma m}\left[(1+G\gamma)\,\vec{B}_\perp + (1+G)\,\vec{B}_\parallel - \left(G\gamma + \frac{\gamma}{\gamma+1}\right)\vec{\beta}\times\frac{\vec{E}}{c}\right].\end{aligned} \tag{4.12}$$

Consider the precession of the particle's momentum induced by the electromagnetic field, the corresponding cyclotron frequency is [18]:

$$\frac{\mathrm{d}\vec{p}}{\mathrm{d}t} = \vec{\Omega}_{cyc} \times \vec{p}, \tag{4.13}$$

$$\vec{\Omega}_{cyc} = -\frac{q}{\gamma m}\left(\vec{B}_{\perp} - \frac{\vec{\beta} \times \vec{E}}{\beta^2 c}\right). \tag{4.14}$$

4.3. Frozen spin method

By comparing the two equations (4.12, 4.14), it can be seen that there is a crossing point in pure electric rings. At this point, the precession frequencies of the momentum vector and the spin vector are equal. If the spin vector starts in the same direction as the momentum vector, then the spin vector will always remain aligned with the momentum vector. This configuration is called the "frozen spin". [13, 23]

$$\begin{aligned}\Delta\vec{\Omega}_{MDM} &= \vec{\Omega}_{MDM} - \vec{\Omega}_{cyc} \\ &= -\frac{q}{\gamma m}\left[G\gamma\vec{B}_{\perp} + (1+G)\,\vec{B}_{\parallel} - \left(G\gamma - \frac{\gamma}{\gamma^2-1}\right)\vec{\beta} \times \frac{\vec{E}}{c}\right].\end{aligned} \tag{4.15}$$

For protons with $G = 1.79$, the corresponding magic momentum is given as:

$$\left(G\gamma - \frac{\gamma}{\gamma^2-1}\right) = 0 \qquad \Rightarrow \qquad p = \frac{mc}{\sqrt{G}} \approx 0.7 GeV/c. \tag{4.16}$$

For particles with negative G, such as deuterons, frozen spin cannot be achieved in pure electric field accelerators. However, for combined bending fields, there is no such restriction. The spin motion of all particles can be frozen as long as the electromagnetic field meets the following conditions [24]:

$$B = \frac{E\beta}{G}\left(\frac{1}{\gamma^2-1} - G\right), \tag{4.17}$$

$$E = \frac{\gamma m \beta^2}{q\rho}\frac{1}{\left(\frac{1}{\gamma^2-1} - G\right)\frac{\beta^2}{G} + 1}, \tag{4.18}$$

$$B = \frac{\gamma m \beta^2}{q\rho}\frac{\left(\frac{1}{\gamma^2-1} - G\right)}{\left(\frac{1}{\gamma^2-1} - G\right)\frac{\beta^2}{G} + 1}\frac{\beta}{G}. \tag{4.19}$$

4.4. Spin tune

When the reference particle travels on a magnetic ring, the particle is only affected by the bending magnetic field of the dipole magnets and the accelerating electric field in the RF cavity. The particle will not experiences any quadrupole fields. Since the direction of the accelerating electric field is parallel to the velocity, $\vec{E}$ also does not

contribute to the precession. One can simplify the Thomas-BMT equation for spin motion as [33]:

$$\frac{\mathrm{d}\vec{S}}{\mathrm{d}t} = -\frac{q}{\gamma m}(1+G\gamma)\vec{B}_{\perp} \times \vec{S}. \tag{4.20}$$

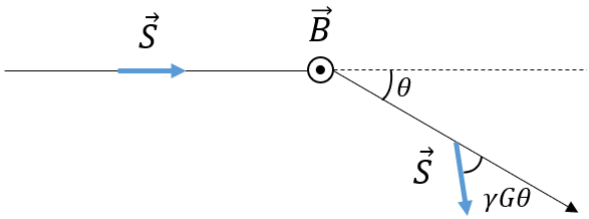

Figure 4.1.: Spin rotation passing through a magnetic bending field. $\vec{B}$ is the external magnetic field and $\vec{S}$ is the spin vector. $(1+\gamma G\theta)$ angle represents a superposition of the spin motion and the beam motion. Adapted from [33].

Figure 4.1 shows spin rotation passing through a dipole field. The orbit bends by an angle θ as it passes through the dipole field. At the same time, the spin rotates around $\vec{B}$ by a $(1+\gamma G\theta)$ angle, which is a $\gamma G\theta$ angle relative to the orbit. In analogy to the definition of the betatron tune, the spin tune is defined as the number of precessions in one orbital revolution [3, 4]:

$$\nu_s = \gamma G. \tag{4.21}$$

4.5. Spin resonance

The spin motion is affected by the perturbation field due to the repetitive motion of the particle in a circular accelerator. On the one hand when the spin motion is far from resonance, the perturbation of the spin motion is incoherent with the spin precession and the total kicks on the spin vector can be averaged out to zero. On the other hand, when the spin motion is in resonance, the kicks on the spin vector are coherently added and leading to depolarization. In order to achieve a long spin coherence time, it is very important to be away from the resonances.
According to the sources of spin resonance they can be classified as imperfection resonance, intrinsic resonances and resonances due to higher-order effects. The information in this section is mainly taken from [8].

imperfection resonance

The condition of the imperfection resonance is:

$$G\gamma = integer. \tag{4.22}$$

Imperfection resonances are caused by magnetic field errors and the misalignment of the magnets. After a particle has completed one revolution around a circular accelerator the error field will repeat. If the precession of the spin vector around its closed orbit is an integer number of turns, the error field will disturb the spin motion in each turn.

intrinsic resonance

The condition of the intrinsic resonance is:

$$G\gamma = kP \pm Q_y \tag{4.23}$$

where k is an integer and Q_y is the vertical betatron tune. P represents the superperiodicity of the lattice i.e. the number of identical periods of the accelerator. The intrinsic resonance is induced by the horizontal fields for vertical focusing. Such resonances are called intrinsic resonances since they are not related to any imperfection but only to betatron motions. Their strength depends on the amplitude of the vertical betatron oscillation.

higher-order resonance

The condition of the higher-order resonance is:

$$G\gamma = k \pm lQ_x \pm mQ_y \pm nQ_s \tag{4.24}$$

where k, l, m and n are integers, Q_x is the horizontal betatron tune, Q_y is the vertical betatron tune and Q_s is the longitudinal tune. This resonance is arising from higher-order field errors of magnets as well as the synchrotron sidebands.

4.6. Spin coherence time

Spin decoherence arises mainly from the difference in momentum between individual particles in the beam. Figure 4.2 illustrates the depolarization of a horizontally polarized beam. For horizontally polarized particles, the decoherence of the spin leads to a uniform distribution of the spin direction in the horizontal plane which in turn reduces the total polarization. To describe the lifetime of the initial polarization, the spin coherence time (SCT) is defined as the time for the total spin polarisation to fall below 1/e.

4.6.1. Orbit lengthening

Spin tune is energy dependent. When the momentum of a particle slightly changes, it leads to a change in spin tune. If the beam is unbunched, this first-order effect is significant due to the large spread of revolution frequencies between the particles. The spin tune spread $\Delta\nu_s$ can be expressed as:

$$\Delta\nu_s = G\Delta\gamma = G\gamma\beta^2\frac{\Delta p}{p_0}. \tag{4.25}$$

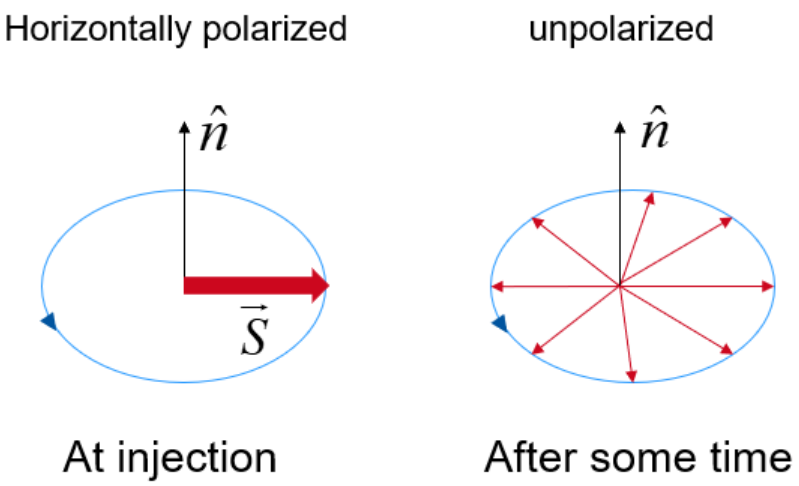

Figure 4.2.: The left picture shows that at the injection the beam is horizontally polarised and all the spins are along the same direction. The right picture shows that after some time the spins spread out in the horizontal plane as the different particles have different velocities. Adapted from [17].

For a bunched beam, the RF cavity drives the particles to oscillate around a reference particle within the bunch. In this way the overall momentum spread can be averaged out and the first-order effect is suppressed by the RF field. The second-order effect dependent on orbit lengthening is one of the sources for the spin tune spread. [23] The orbit lengthening due to the betatron motion is [15]:

$$\left(\frac{\Delta C}{C_0}\right)_\beta = -\frac{2\pi}{C_0}(\varepsilon_x \xi_x + \varepsilon_y \xi_y), \tag{4.26}$$

where ε_x and ε_y refer to the emittance in the horizontal and vertical plane respectively, ξ_x and ξ_y refer respectively to the horizontal chromaticity and vertical chromaticity. The contribution of the momentum deviation $\Delta p/p_0$ to the orbit lengthening is [15]:

$$\left(\frac{\Delta C}{C_0}\right)_{\Delta p} = \alpha_0 \frac{\Delta p}{p_0} + \alpha_1 \left(\frac{\Delta p}{p_0}\right)^2 + ..., \tag{4.27}$$

where α_n is n-th order momentum compaction factor.

4.6.2. Sextupole correction

Sextupole magnets can be used to minimise the spin decoherence caused by betatron motions and the momentum spread. One can use a sextupole with strength k_s to correct the second-order momentum compaction factor α_1 [19]:

$$\Delta\alpha_1 = -\frac{k_s \cdot D_0^3}{C_0} \tag{4.28}$$

where D_0 is the first-order dispersion function and C_0 is the circumference.

Simultaneously the effect of the sextupole on the orbit lengthening is [19]:

$$\left(\frac{\Delta C}{C_0}\right)_{sext} = \mp \frac{k_s D_0 \beta_{x,y} \varepsilon_{x,y}}{C_0}, \tag{4.29}$$

here $\beta_{x,y}$ denotes to the beta function in the horizontal and vertical plane respectively. The minus and plus sign represent orbit lengthening due to horizontal and vertical plane effects respectively.

5. Simulation model

In this chapter, the first part describes the accelerator complex at the Institut für Kernphysik (IKP) Forschungszentrum Jülich. Second, the implementation and benchmarking of the model used in this thesis is presented. Finally, algorithms for calculating spin tune are discussed.

5.1. The Cooler Synchrotron COSY

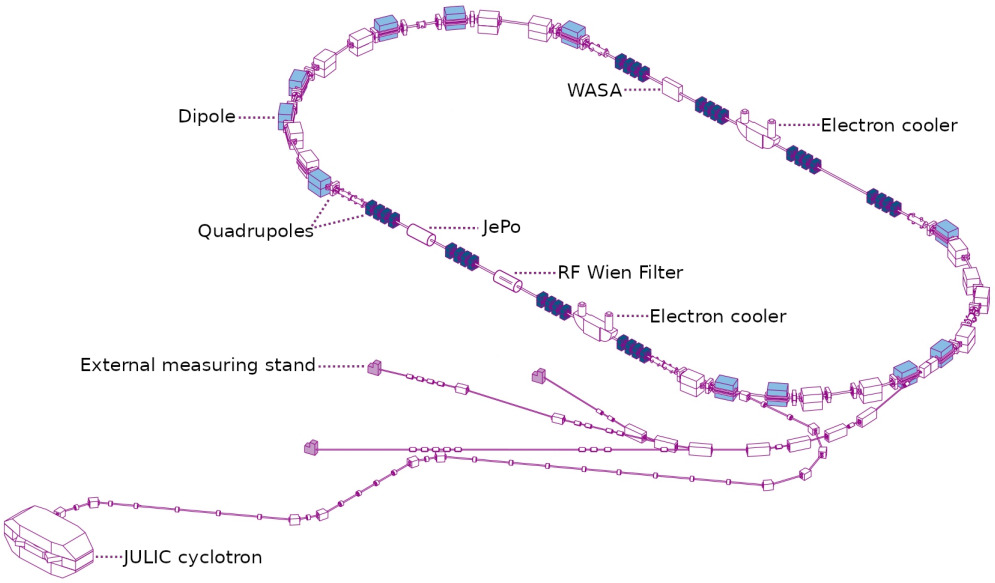

Figure 5.1.: Schematic of the Cooler Synchrotron COSY and the pre-accelerator JULIC including dipoles, quadrupoles, JePo polarimeter, RF Wien filter, electron cooling system and WASA detector. Taken from [27]

The accelerator complex consists of polarized or unpolarized ion sources providing protons H^- or deuterons D^-, the cyclotron JULIC as a pre-accelerator and the Cooler Synchrotron COSY. The schematic overview of the accelerator complex is shown in Figure 5.1.

At the cyclotron JULIC, H^- and D^- can be accelerated up to a momentum of 300

MeV/c and 600 MeV/c respectively. The ions are then guided to the synchrotron via a 100 m long beam line. COSY has the ability to accelerate proton and deuteron beams in the momentum range between 0.3 GeV/c and 3.65 GeV/c [14]. In order to reduce the momentum spread of the beam and shrink the transverse equilibrium phase space, COSY use electron cooling for proton beams with momentum up to 0.6 GeV/c and stochastic cooling for those with momentum above 1.5 GeV/c.[10]
The circumference of COSY is about 184 m with two 180° arc sections and two straight sections. In each 52 m long arc section, 12 dipoles that bend the beam are distributed. In addition, 12 quadrupoles are also located in each arc section, forming three mirror-symmetric cells together with the dipoles. The structure of each unit is made up of DOFO-OFOD. Here O is a bending dipole, F and D refer to focusing and defocusing quadrupoles (MQU1 to MQU6) respectively.[9]
Each 40 m long straight section contains $4 \times 4 = 16$ quadrupoles (MQT1 to MQT8), placing in the FDDF or DFFD configuration, which make up two mirror-symmetric telescopes. 7 sextupoles, an RF cavities, and 2 polarimeters (WASA and JePo) are installed on the straight sections. In addition, important devices for manipulating the spin of polarized beams, such as a RF solenoid, a Siberian Snake and an RF Wien filter are also located in the straight sections.

5.2. Bmad model of COSY

In this thesis, the Bmad software library was used to simulate beam and spin dynamics for charged particles in the Cooler Synchrotron COSY. Bmad was developed in the 1990s by Cornell University's Laboratory for Elementary Particle Physics. The Bmad code is an open source, object-oriented library written in Fortran 2008. It has several tracking algorithms such as Runge–Kutta and symplectic (Lie algebraic) integration. [35]
Although Bmad lattice uses a MAD like syntax, Bmad cannot read MAD files directly. One need to convert the existing COSY optics files output by MAD-X into Bmad lattice file syntax. As the .twiss file are output in s-coordinate order, where s is the position along the reference orbit. Python was used to read it line by line and sort all the elements into multiple .bmad files.[36] This is particularly conducive to updates and modifications. Bmad's built-in routines will parse the lattice and create a digested file so that programs using the same lattice file can read the digested file again to save time. The COSY lattice includes the following files:

- **cosy_actions.bmad**: initializes the species, number and momentum of particles, whether the cavity is on or not and the default tracking method used.
- **cosy_lattice.bmad**: defines the sequence of elements that make up COSY.
- **element_layout.bmad**: lists all elements and their attributes.
- **element_attributes.bmad**: controls kicker magnets, solenoids and RF cavities.
- **magnet_groups.bmad**: magnets that use the same power supply are grouped into one family. This file includes 8 of straight section quadrupoles, 6 of arc

section quadrupoles and 3 of arc section sextupoles.

- **magnet_settings.bmad**: sets magnet strengths for different families.

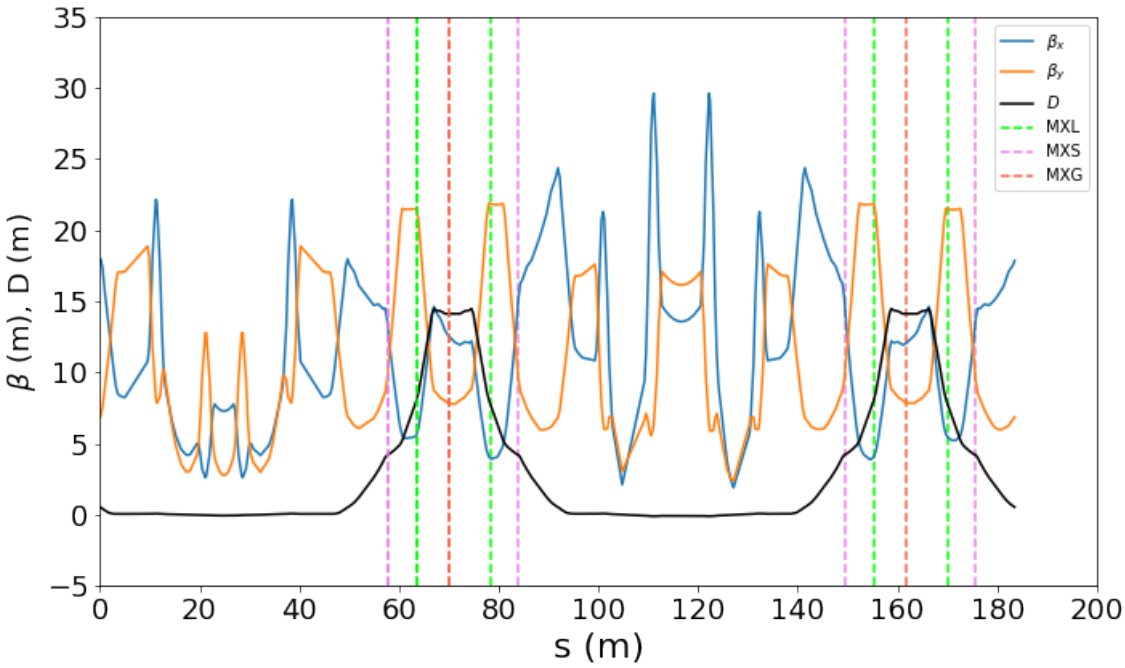

Figure 5.2.: Optical functions of the Cooler Synchrotron COSY. The betatron tunes are (Q_x = 3.63, Q_y = 3.72) and the natural chromaticities are (ξ_x = −4.25, ξ_y = −3.94).

The idealized COSY lattice is from the second precursor run experiment, where misalignments of the magnets are not taken into account, the transverse betatron tunes are (Q_x = 3.63, Q_y = 3.72) and the natural chromaticities are (ξ_x = −4.25, ξ_y = −3.94) when all sextupoles are turned off. Figure 5.2 shows the optical functions such as horizontal β_x and vertical β_y beta functions as well as the dispersion D_x of the lattice. The horizontal coordinate is the position s along the accelerator. The dispersion $D = 0$ in the straight section is a typical setting for COSY, which facilitates the placement of experimental devices. In the arc sections where D is not zero, three different families (MXG, MXS, MXL) of sextupoles are installed, which are indicated in the plot by vertical lines of different colours.

5.3. Benchmarking of the COSY model

5.3.1. Phase space in Bmad

After the COSY's model was implemented in Bmad, it is important to benchmark the model. Bmad uses a canonical coordinate system [35]

$$r(s) = (x, p_x, y, p_y, z, p_z), \tag{5.1}$$

where s is the distance of the reference particle relative to the zero point of the reference orbit (sometimes called the design orbit). The x-axis and y-axis indicate the offsets of the particle in the transverse plane, respectively. The phase space momenta p_x and p_y are derived from the corresponding momentum P_x and P_y, normalised by the reference momentum P_0:

$$\begin{aligned} p_x &= \frac{P_x}{P_0} \\ p_y &= \frac{P_y}{P_0}. \end{aligned} \tag{5.2}$$

The longitudinal z-axis is defined as:

$$\begin{aligned} z(s) &= -\beta(s)c(t(s) - t_0(s)) \\ &= -\beta(s)c\Delta t(s) \end{aligned} \tag{5.3}$$

where β is the ratio of v/c with v being the particle's velocity, $t(s)$ and $t_0(s)$ represent respectively the time when the particle and the reference particle arrive at the position s.

For relativistic particles, the velocity of the particle and the velocity of the reference particle are both the speed of light. Then βct represents the path length L, and the change of z can be expressed as :

$$\Delta z = L_0 - L_p \tag{5.4}$$

where L_p and L_0 refer to the path length of the particle and the reference particle.

In the next part, the phase space ellipses of offset particles were investigated. Using a single proton with a momentum of 531 MeV/c, which have small deviations in x, y and momentum respectively. Tracking it for 2,000 turns in Bmad, at the beginning of each turn one can always recorded the six phase space coordinates of the particle in the first element. These data was used to plot three phase spaces in transverse and longitudinal planes.

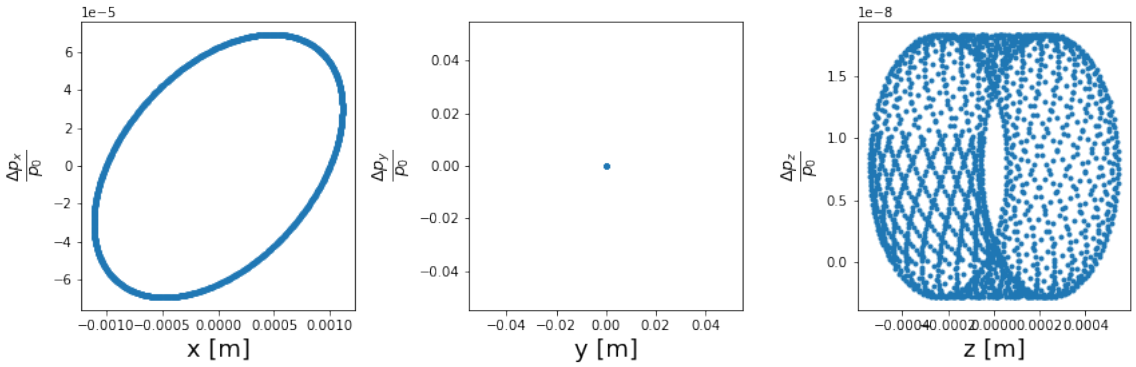

Figure 5.3.: The three-dimensional phase space of a particle with an initial horizontal offset. The offset is set to $\Delta x = 1$ mm mrad. The left plots shows the horizontal phase space ellipse. The middle plot shows that motion in the vertical plane is not affected. The ellipses shift due to the dispersion effect are shown in the right plot.

For a particle with only an initial offset in the horizontal x-direction, its three-dimensional phase spaces are shown in Figure 5.3. The left plot of the figure shows a stable phase space ellipse in the horizontal plane. The middle plot shows that in an ideal lattice the horizontal plane is decoupled with the vertical plane, so that the motion in the vertical plane is not affected. Due to the path length change caused by the dispersion effect, the phase of the particle does not match the cavity's phase. The right plot illustrates that the centers of the ellipses are shifted.

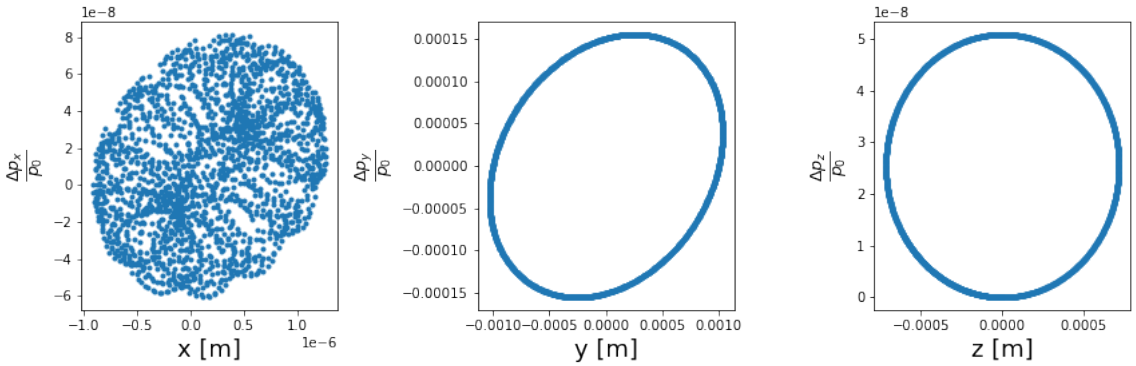

Figure 5.4.: The three-dimensional phase space of a particle with an initial vertical offset. The offset is set to $\Delta y = 1$ mm mrad. The middle and right plots show the vertical and the longitudinal phase space ellipses respectively. The left plot shows small perturbations in the horizontal plane.

In Figure 5.4, the particles have an initial vertical offset. Deviations in the vertical plane would cause orbit lengthening via betatron motions. In the longitudinal plane, the phase of the particles does not match the cavity's phase, causing small deviations

in the longitudinal direction as well. Due to the dispersion effect, this ends up creating some small perturbations in the horizontal plane as well, although the horizontal and vertical planes are decoupled.

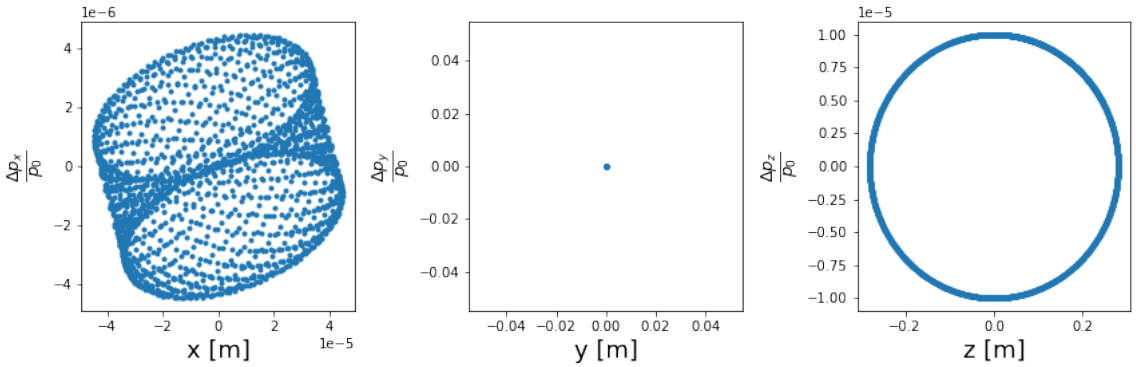

Figure 5.5.: The three-dimensional phase space of a particle with an initial momentum deviation. The offset is set to $\Delta p/p_0 = 10^{-5}$. The left plots shows the horizontal phase space ellipses shift due to the dispersion effect. The middle plot shows that motion in the vertical plane is not affected. The left plots shows the longitudinal phase space ellipse.

When there is a small deviation in the momentum of the particle, one can clearly see in Figure 5.5 that there is a large impact on the motion in the horizontal plane due to the dispersion effect, while the vertical plane is unaffected. The cylindrical shape in the left plot is formed by large shifts in the phase space ellipses. It is also worth noting that the distortion of the phase space ellipse caused by the deviations from the longitudinal plane, i.e. the momentum deviations, is much greater than the offsets in the transverse planes.

5.3.2. Spin tune of a proton

The spin motions of the reference particle in horizontal plane and longitudinal plane are shown in Figure 5.6. Since the initial spin is aligned with the longitudinal direction, the spin precession will only happen in the horizontal plane. The simulation results show that there is no spin motion in the vertical plane. In the horizontal and longitudinal planes, however, regular periodic changes of the particle's spin can be observed as shown in the left and right plots.

It is important to know how Bmad processes the spin tune. The Bmad subroutine Closed_orbit_calc can uses 1-turn transfer matrix to calculate the spin tune. It reads the initial spin vector of the particle, and after one turn, records the spin vector at the same position. The angle between the two vectors is calculated via a built-in mathematical routine and divided by 2π to obtain the fractional part of the spin tune. According to Equation 4.21 $\nu_s = \gamma G$, the theoretical spin tune of the proton can be obtained:

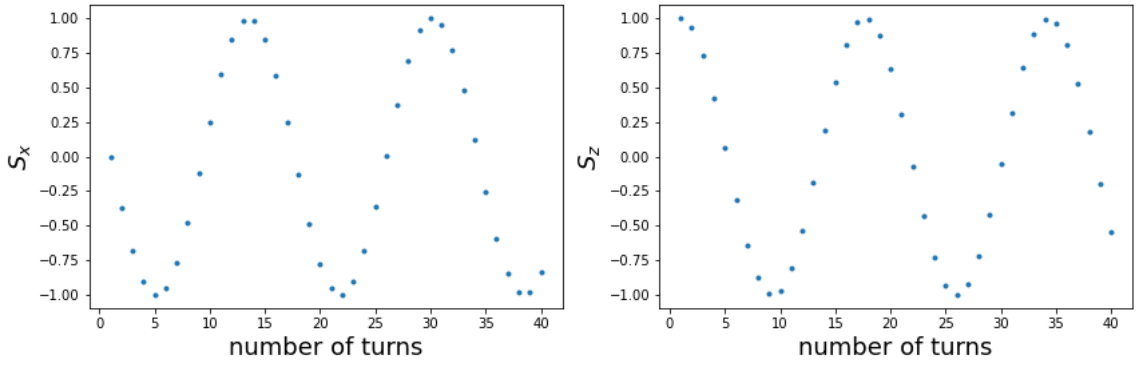

Figure 5.6.: Spin motions of the reference particle in horizontal plane (left) and longitudinal plane (right). The initial spin vector is aligned with the momentum vector, parallel to the longitudinal direction. The spin precesses in the horizontal plane. The x-axis is the number of tracking turns. The y-axis is the component of the spin vector in the horizontal or longitudinal directions.

$$Theory : \nu_s = +2.0600441688281070$$
$$Bmad : \nu_s = -0.0600441688257620.$$

The calculated value agrees with the theoretical value to the 11th digit. The calculations show that the Bmad routine is able to accurately calculate the spin tune of a particle after completing one revolution. This also demonstrates that the Bmad program can simulate the spin motion of a particle in a circular accelerator very well. However, it is not sufficient to investigate the spin tune spread by using one turn of the spin tune difference from the theoretical value. As the number of turns is increased, the spin tune spread due to the orbit lengthening becomes larger and larger. In order to properly study the SCT, in this thesis the average spin tune spread is usually calculated using data tracking more than 1,000 revolutions.

5.4. Algorithm for spin tune

5.4.1. Method for the reference particle

5.4.1.1. Fitting method

Observing the regular motion in Figure 5.6, one can apply a sinusoidal fit to the spin component in either the horizontal or longitudinal direction to obtain the spin tune. The fitting results in the horizontal direction is shown in Figure 5.7, where the second parameter b is the frequency ω_{fit} of this sinusoidal function. One can calculate the spin tune by using the following equation:

$$\nu_s = \frac{\omega_{fit}}{2\pi}. \tag{5.5}$$

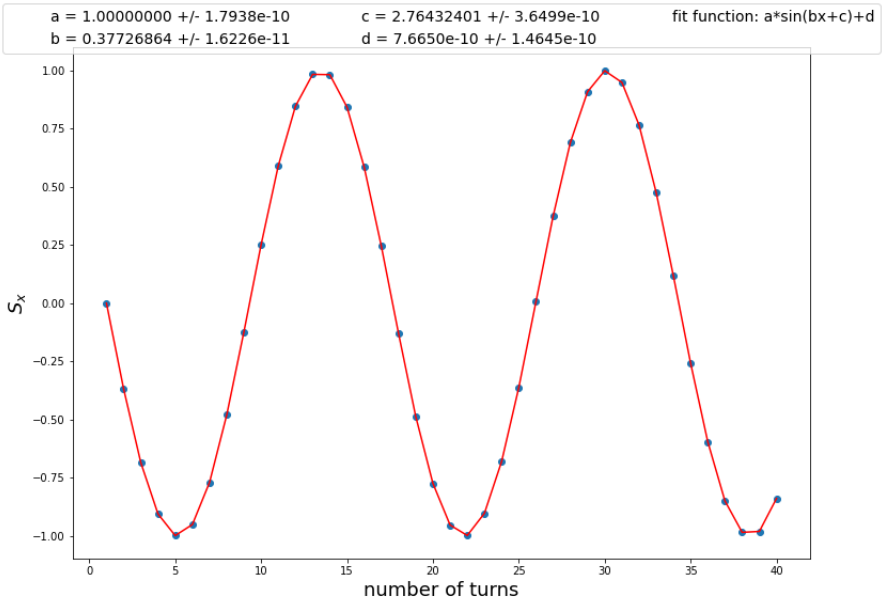

Figure 5.7.: The horizontal spin direction is plotted versus the turn number. A sinusoidal function is fitted. The function and parameters used for the fit are shown in the legend. The blue dots are the simulated data and the red line is the fitted curve.

By tracking the reference particle for 40 turns and using the fitting method one can get:

$$Theory : \nu_s = 2.0600441688281070$$
$$Fitting : \nu_s = 0.0600441688264975 \pm 2.5824 \cdot 10^{-12},$$

the fitted value agrees with the theoretical value to the 11th digit.

5.4.1.2. Average phase advance (APA) method

A commonly used method of calculating the frequency of an orbit in simulations is the average phase advance (APA) method.[7] The spin tune is given by the average of phase advance angle θ_i :

$$\nu_s = \frac{1}{2\pi(n-1)} \sum_{i=2}^{n} \theta_i \tag{5.6}$$

where θ_i denotes the phase advance between the turn $(i-1)$ and the turn i.
When v_1 and v_2 are used to represent the spin vector of a particle, the Equation 5.6 becomes:[31]

$$\nu_s = \frac{1}{2\pi(n-1)} \sum_{i=2}^{n} cos^{-1}\left(\frac{\vec{v_1} \cdot \vec{v_2}}{|\vec{v_1}||\vec{v_2}|}\right) \tag{5.7}$$

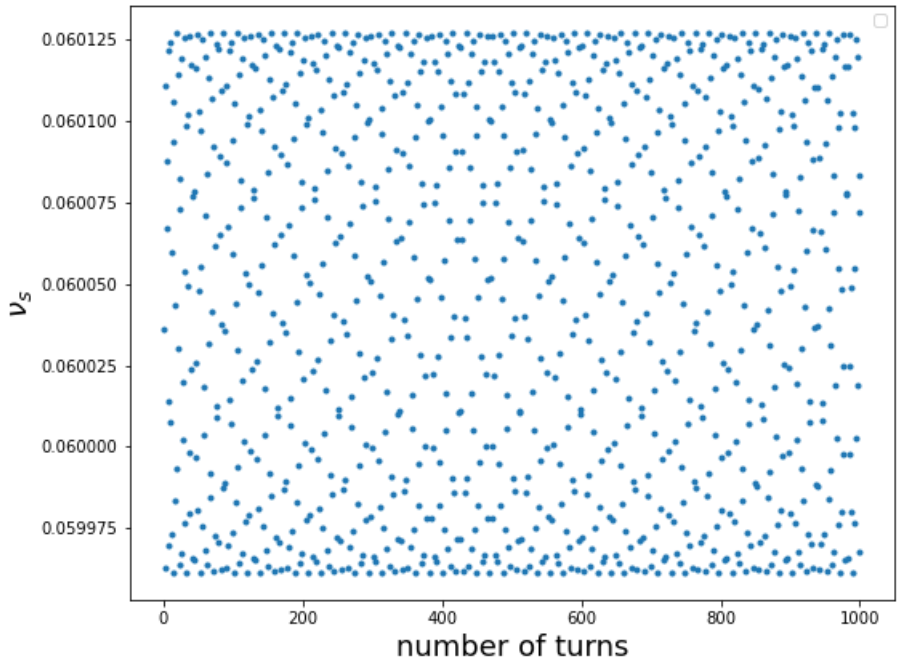

Figure 5.8.: Spin tune distribution of a particle with an initial horizontal offset Δx = 1 mm mrad. Due to the betatron motion and dispersion effects, the particle undergoing synchrotron oscillation in the longitudinal plane leads to spin tune spread. The blue dots denote the spin tune for each turn calculated via the APA method.

By tracking the reference particle for 40 turns and using the fitting method one can get:

$$Theory : \nu_s = 2.0600441688281070$$
$$APA : \nu_s = 0.0600441688258315 \pm 3.8471 \cdot 10^{-14},$$

here, the standard deviation of spin tunes is used as the error. The spin tune obtained via APA method agrees with the theoretical value to the 11th digit.

5.4.2. Method for offset particles

5.4.2.1. Betatron and synchrotron effects

The previous discussion was based on the reference particle, however, for particles with deviations, there are difficulties with the two algorithms above where high accuracy is required. Figure 5.8 shows a particle has an initial horizontal direction offset Δx. After tracking for 10,000 turns, its spin tunes calculated by the average phase advance method are evenly distributed within a specific range. This is a result of the combined betatron motion and dispersion effects, which can be largely averaged out.
For a particle with an initial momentum deviation $\Delta p/p$, also tracking for 10,000

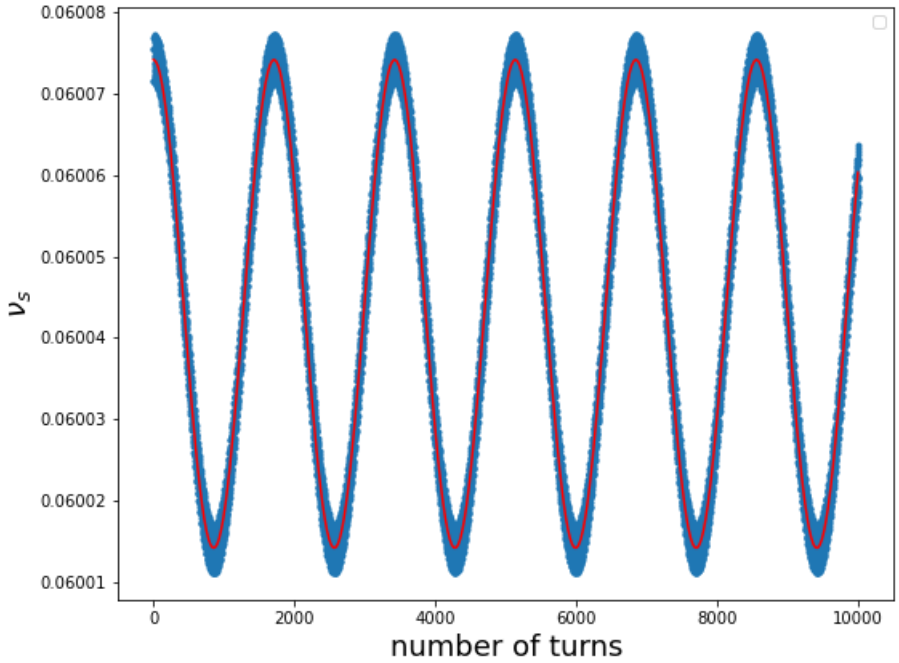

Figure 5.9.: Spin tune distribution of a particle with an initial momentum deviation $\Delta p/p = 10^{-5}$. The synchrotron oscillation strongly modulates the spin tune. The frequency of the synchrotron oscillation can be obtained by applying a sine fit function (the red curve). The blue dots denote the spin tune for each turn calculated via the APA method.

turns, the distribution of spin tune is shown in Figure 5.9. Due to the cavity, one can clearly see the synchrotron oscillation modulates the spin tune results. Applying a sinusoidal fit to the spin tunes yields a frequency of 400 Hz approx., which is consistent with the synchrotron frequency. This effect cannot be averaged out for a beam with large numbers of particles, and one have to find a new algorithm to calculate the spin tune.

5.4.2.2. Fast Fourier transform (FFT) method

Another method commonly used in measurement is based on Fourier analysis.[7] The Fourier transform is a mathematical operation, which transform time-domain data of an observable into frequency-domain. In our case, it is a transformation from the turn to the tune. The following three plots (Figure 5.10 and Figure 5.11) show the spin tune spectra of particles with horizontal x, vertical y and momentum deviations $\Delta p/p$ respectively. Each particle was tracked for 10,000 turns.
As the data are obtained from simulations, they are noise-free. The frequency, i.e., the spin tune can be determined as the horizontal coordinate of the main peak in the amplitude spectrum. In Figure 5.10, there are only deviations in the transverse plane. The plots show that there is only one peak, whose x-axis is exactly the fractional part of the theoretical value. When a particle only has the momentum deviation $\Delta p/p$, as

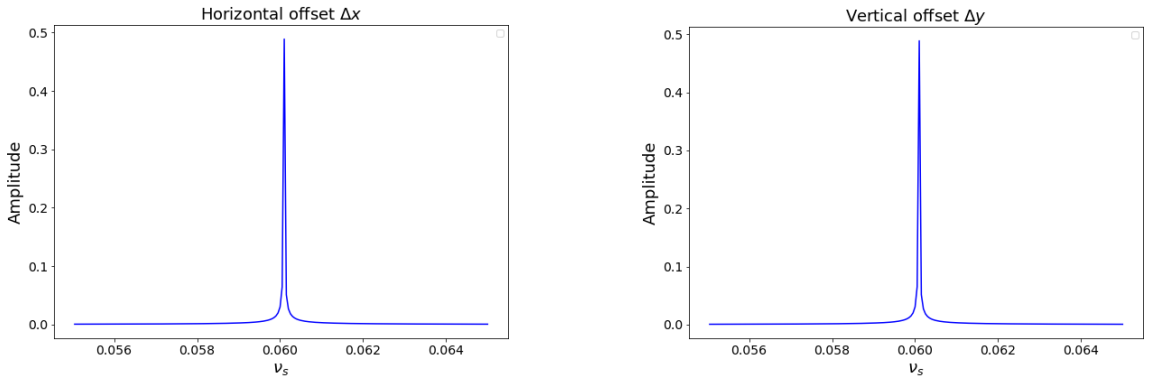

Figure 5.10.: The simulated spin tune spectra for particles with horizontal offsets (left) and vertical offsets (right). The x-axis is the spin tune and the y-axis is the normalised amplitude.

shown in Figure 5.11. Some sidebands with smaller amplitude appear near the main peak. Similarly, the x-axis of the main peak is the fractional part of spin tune, while those of the sidebands are shifted due to synchrotron modulation.
The frequency resolution is the difference in frequency between each bin. Since the spin tune is the number of spin precessions per revolution. In a fast Fourier transform (FFT), the spin tune resolution is defined as

$$\Delta\nu_s = \frac{F_s}{N}, \tag{5.8}$$

where F_s is the sample frequency, N is number of data points used in the FFT. This is not enough to precisely determine spin tunes in the simulation results.
To improve the resolution, many methods have been proposed. One of them, called numerical analysis of fundamental frequencies (NAFF) algorithm, is widely used in today's accelerator measurements and simulations. The NAFF code was developed in the 1990s as a method to analyse chaotic dynamical systems.[6] The resolution of NAFF algorithm can get up to $1/N^4$ for noise free data in simulations.[29] Moreover, this method is very easy to use in python because there are scientists from CERN who have implemented this python module.[37] The NAFF method is not only suitable for analysing the reference particles, but also to the particles with deviations. In addition, another advantage is that it runs very fast compared to the average phase advance method.

By tracking the reference particle for 10,000 turns and using the FFT/NAFF method one can get:

$$Theory : \nu_s = 2.0600441688281070$$
$$FFT/NAFF : \nu_s = 0.0600441688257838 \pm 10^{-16},$$

here, the frequency (tune) resolution for noise free simulations data is used as the

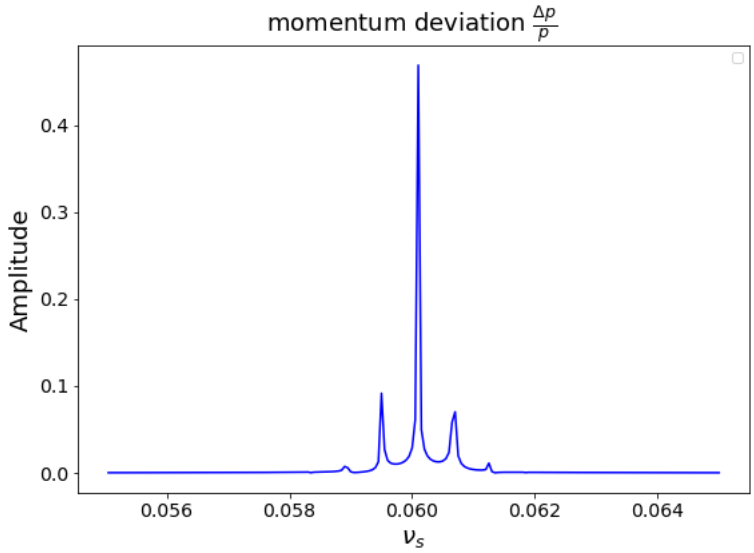

Figure 5.11.: The simulated spin tune spectrum for a particle with an initial momentum deviation $\Delta p/p$. The x-axis is the spin tune and the y-axis is the normalised amplitude. The synchrotron modulations are shown as sidebands around the main peak.

error. The spin tune obtained via FFT/NAFF method agrees with the theoretical value to the 11th digit.

6. Investigation of spin coherence time

6.1. Beam parameters and spin tracking

In this thesis, a large part of the work is the spin tracking simulation of proton beams. We have two approaches to tracking a beam of multiple particles. The first is to use Bmad's macroparticle simulation module to split the beam into bunches for tracking. The advantage of this method is that the space charge and coherent synchrotron radiation effects can be examined. The disadvantage is that it is limited by the performance of the CPU's single core, so only simulations with a small number of particles can be performed, which does not meet the requirements of our experiments. The second method, which is the one we use, ignores the interactions between particles and simulates the individual particles that make up the beam. This method can utilize the multi core CPUs of the cluster and perform parallel computing at the same time, which greatly saves the simulation time.

6.1.1. Beam parameters

There are two standard methods for Bmad-based programs to determine the initial distribution of the beam. One is to use the *beam_init_struct* structure, which contains parameters that can build the particle distribution. Each time the program runs, a beam that satisfies the above parameters is regenerated. This approach introduces more uncertainty to the simulation results due to different random factors. Another method is to specify the initial beam distribution based on a fixed file containing the positions of individual particles satisfying the *beam_init_struct* structure. Using this method ensures that each simulation has the same particle distribution. The second method was used in this thesis. Table. 6.1 shows the initial parameters of a proton beam.

6.1.2. Particle distribution

The next step is to investigate whether the distribution of particles can be maintained consistently within the simulation. First is the initial distribution generated by the subroutine based on *beam_init_struct* structure, as an example in the transverse plane. Figure 6.1 shows histograms of the particle distributions in the horizontal and vertical directions, respectively. In both directions the mean values are very close to zero and far below one standard deviation. This demonstrates that the distributions of the initially generated particles are consistent with the parameter settings.
After tracking one million turns in the default lattice, Bmad records the position information of each particle in the beam. These are plotted separately as histograms in Figure 6.2. One can see that compared to the initial particle distributions, the mean

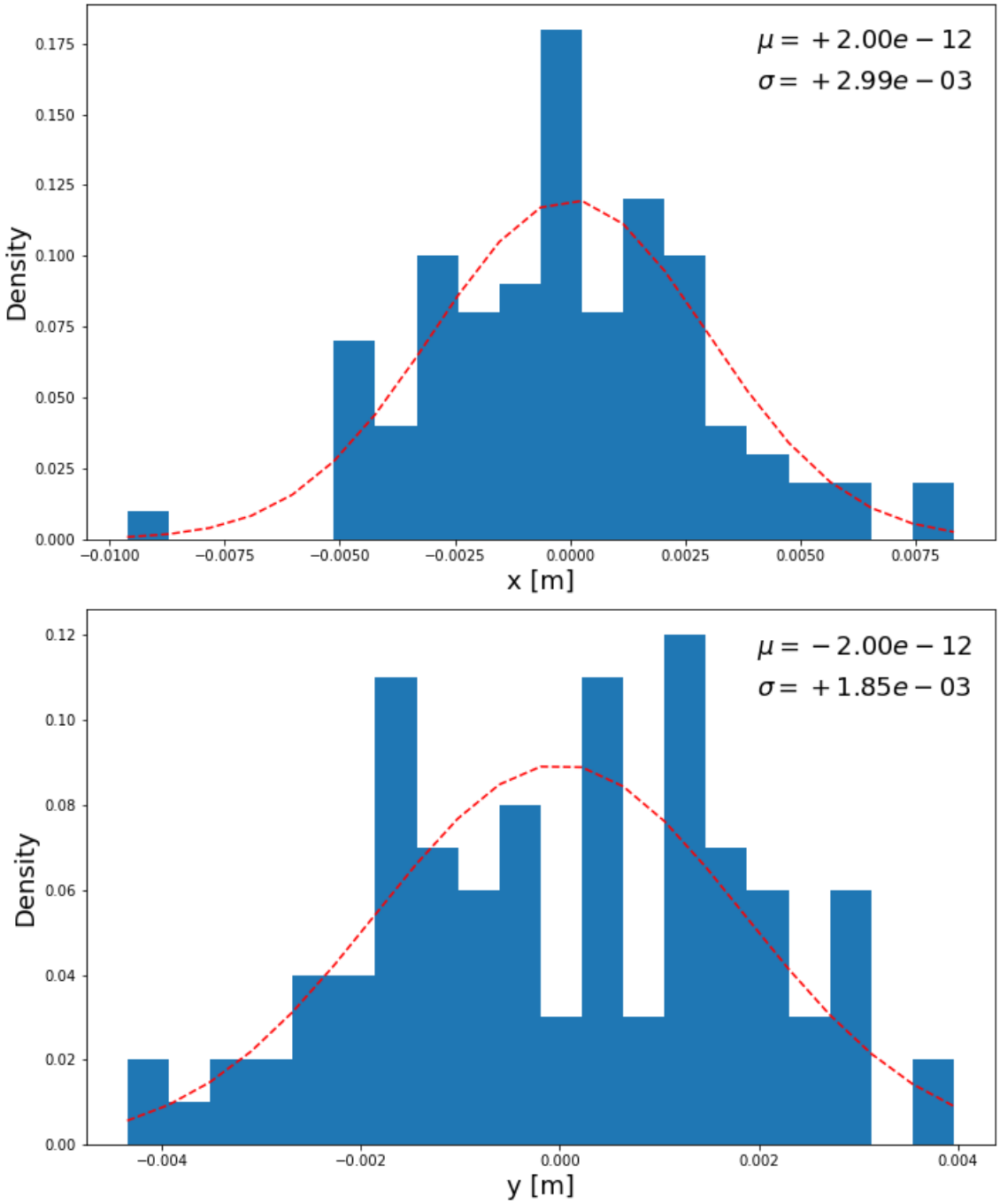

Figure 6.1.: Initial particle distribution of the beam in the horizontal plane (top panel) and in the vertical plane (bottom panel). The x-axis is the distance between the particle and the reference particle, while the y-axis is the normalised probability density function. The red dashed line represents the fitted Gaussian distribution curve.

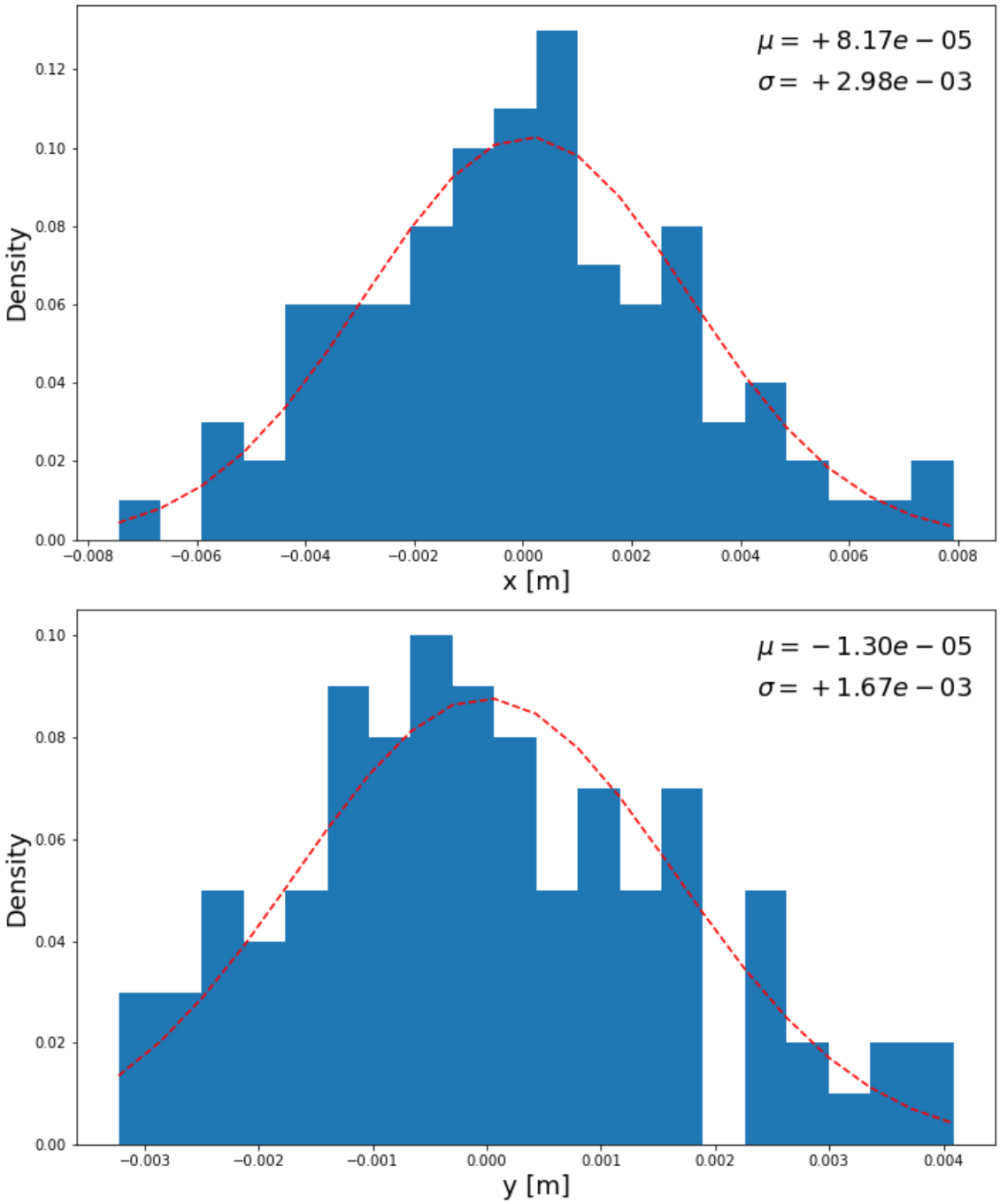

Figure 6.2.: The particle distribution in the horizontal plane (top panel) and in the vertical plane (bottom panel) in the beam after one million revolutions was tracked. The x-axis is the distance between the particle and the reference particle, while the y-axis is the normalised probability density function. The red dashed line represents the fitted Gaussian distribution curve.

species	proton
n_particle	100
n_bunch	1
distribution_type	Gaussian
ε_x	$5 \cdot 10^{-7}\ m \cdot rad$
ε_y	$5 \cdot 10^{-7}\ m \cdot rad$
σ_z	10^{-3}
σ_{pz}	10^{-4}

Table 6.1.: Beam initial parameters. The number of particles in the beam with only one bunch is 100. Within a bunch, the generated particles follow a Gaussian distribution. In the transverse plane, the emittances of x and y are both $5 \cdot 10^{-7}\ m \cdot rad$. In the longitudinal plane, the standard deviation of z is 10^{-3} and σ_{pz} refers to the fractional energy spread dE/E.

values have slightly increased in both horizontal and vertical directions. The increasing in the horizontal direction is more obvious. Since the motion in the horizontal direction is coupled with that in the longitudinal direction. Particles with different initial momentum deviations result in disturbances in the horizontal direction, thus increasing the average value of x. In a real accelerator, the emittance growth is due to the fringe fields, the higher-order fields and the intra-beam scattering effect. In the simulations of this thesis, interactions between particles are neglected and all 'fringe_type' are set to 'none'. So we assume that the emittance growth only comes from the sextupoles as well as statistical fluctuations.

6.1.3. Spin tracking

To investigate the effect of particle number on the spin coherence time (SCT), two separate spin tracking simulations were performed. The default COSY lattice with all sextupoles turned off was used. The particle's position, momentum and spin data at each turn were recorded using the subroutine *track_all*.
Figure 6.3 and 6.4 show the results of the simulations for particle numbers n = 1000 and n = 100, respectively. The x-axis is the time. The y-axis is the total polarization and a red line is drawn at the $y = 1/e$. Comparing the two plots, it can be seen that for n = 1000, total polarization below 1/e appears at $0.093 \pm 0.003\,s$, while for n = 100 at $0.089 \pm 0.006\,s$. By definition, the time at which total polarization falls below 1/e is the SCT. The difference in SCT between the two is very small. When the number of particles is larger, the error is smaller. In order to reduce the simulation computing time, it is sufficient for us to use 100 particles.

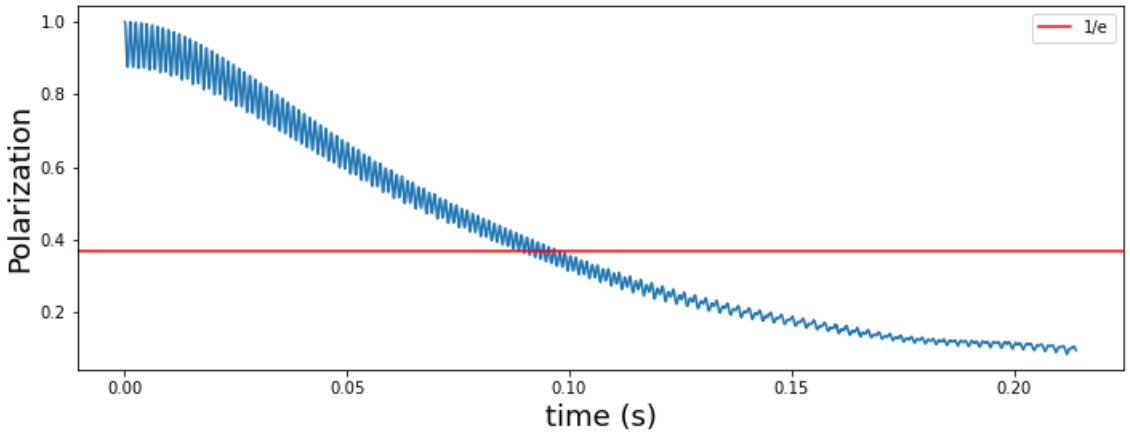

Figure 6.3.: Spin coherence time for a polarized proton beam with the particle number of 1000. The x-axis is the time and the y-axis is the total polarization. A red line indicates that the total polarization drops to 1/e of the initial polarization, and the corresponding time is the spin coherence time.

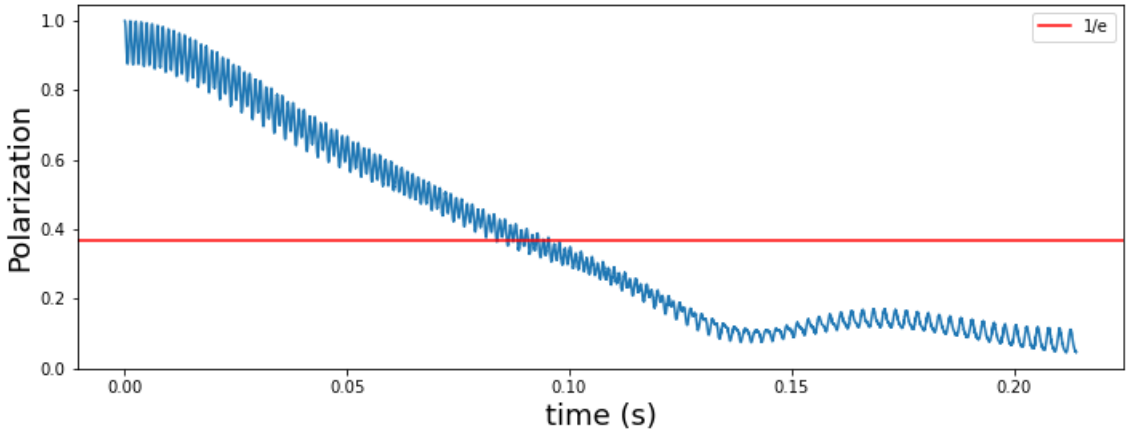

Figure 6.4.: Spin coherence time for a polarized proton beam with the particle number of 100. The x-axis is the time and the y-axis is the total polarization. A red line indicates that the total polarization drops to 1/e of the initial polarization, and the corresponding time is the spin coherence time.

6.2. Dependence of the SCT on phase space parameters

6.2.1. Emittances

Previous work suggested that the SCT is dependent on the emittances and momentum spread of the beam.[22, 26] In order to investigate the relationship between emittances and the reciprocal of SCT, simulations were conducted as follows. First, ε_y was fixed

at $0.1\,mm\,mrad$ and then ε_x was varied from $0.1\,mm\,mrad$ to $0.6\,mm\,mrad$. Spin tracking simulations were performed on them separately and their SCT results were then analysed. All results are presented in Table 6.2.

Table 6.2.: Different emittances and their corresponding SCTs. The first column of table shows the emittance values in the horizontal ε_x or vertical ε_y directions. When varying one, the other emittance is fixed at 1 mm mrad. The second column is the SCT when changing ε_x, and the third column is the SCT when changing ε_y.

ε_x / ε_y	SCT_x	SCT_y
0.1 mm mrad	0.336 ± 0.015 s	0.336 ± 0.015 s
0.2 mm mrad	0.234 ± 0.016 s	0.285 ± 0.024 s
0.3 mm mrad	0.169 ± 0.028 s	0.262 ± 0.021 s
0.4 mm mrad	0.126 ± 0.017 s	0.208 ± 0.016 s
0.5 mm mrad	0.117 ± 0.019 s	0.207 ± 0.016 s
0.6 mm mrad	0.112 ± 0.005 s	0.192 ± 0.008 s

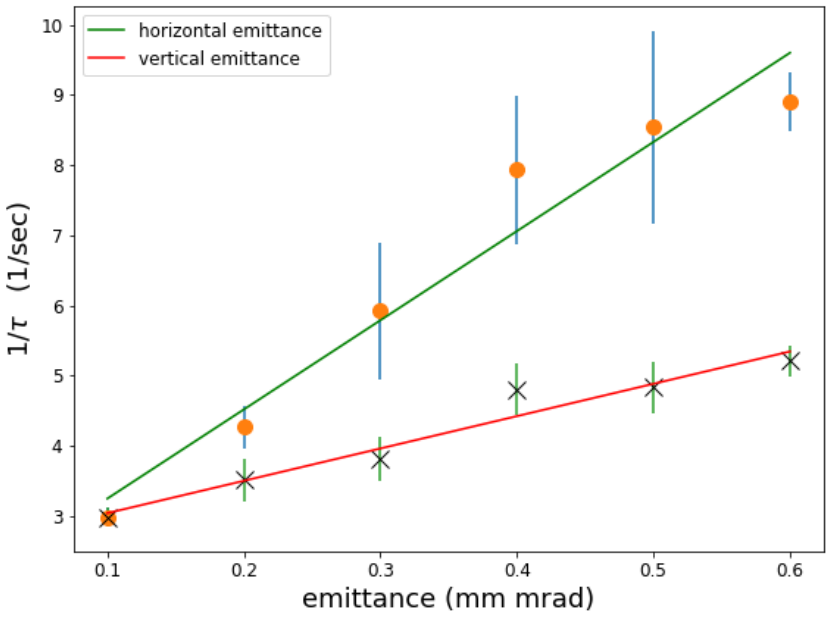

Figure 6.5.: The relationship between emittances and the reciprocal of SCTs. The x-axis is the value of emittances and the y-axis is the inverse of SCTs. The orange dots are the horizontal emittances, the green line is the applied linear fit. The black crosses are the vertical emittances, the red line is the applied linear fit.

The results in Table 6.2 are plotted in Figure 6.5. The inverse of SCT was chosen because it is proportional to the spin tune spread $\Delta\nu_s$. One can see from the plot that $1/\tau$ fits well linearly with the emittances in both directions. To obtain a long SCT,

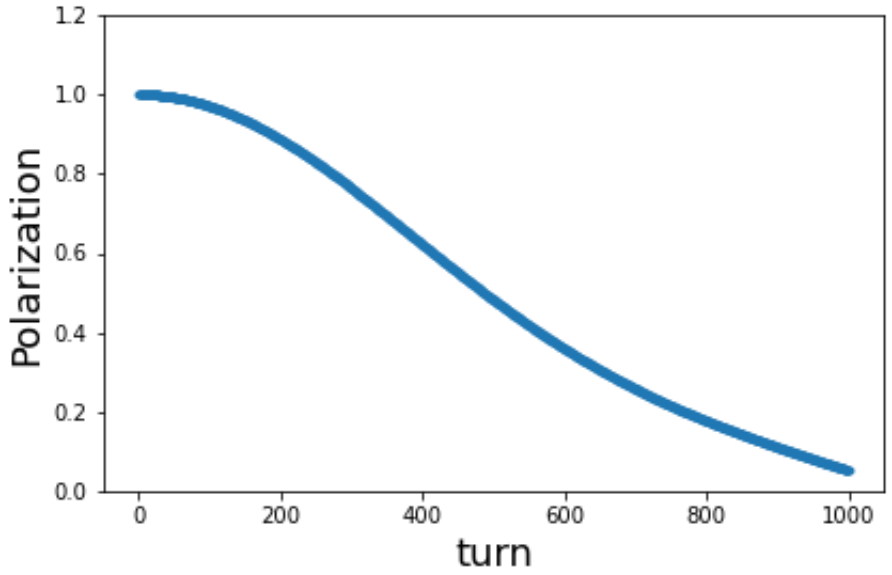

Figure 6.6.: The polarisation lifetime of a proton beam when the cavity is turned off. The x-axis is the revolutions and the y-axis is the total polarization.

small emittances are needed. In real experiments, one needs to reduce the emittance by employing beam cooling.

6.2.2. Momentum spread

As discussed in Section 4.6.1, the first order momentum spread effect can be expressed as Equation 4.25:

$$\Delta\nu_s = G\Delta\gamma = G\gamma\beta^2\frac{\Delta p}{p_0}.$$

Figure 6.6 shows a unbunched proton beam, the overall polarisation drops rapidly to zero within one thousand turns. The first order effect can be removed by turning on the cavity and bunching. After removing the first order effect, the polarisation will be maintained for a much longer time.

In order to investigate the relationship between the second-order effect of momentum deviation and the SCT, one can vary $\Delta p/p$ and then performed spin tracking simulations. The results are presented in Table 6.3, where the emittance in both x and y directions are fixed at $0.1\,mm\,mrad$. Figure 6.7 shows that the inverse of SCT is linearly related to the square of the momentum deviation. Note that this only holds when the momentum offset Δp is very small. Otherwise, the particle will be lost when Δp is greater than a certain value.

$\Delta p/p$	0.5×10^{-4}	1.0×10^{-4}	1.5×10^{-4}	2.0×10^{-4}
SCT (s)	0.416 ± 0.017	0.375 ± 0.029	0.268 ± 0.033	0.231 ± 0.049

Table 6.3.: Different momentum spreads and SCTs. The first row is the momentum spread and the second row is the corresponding SCT.

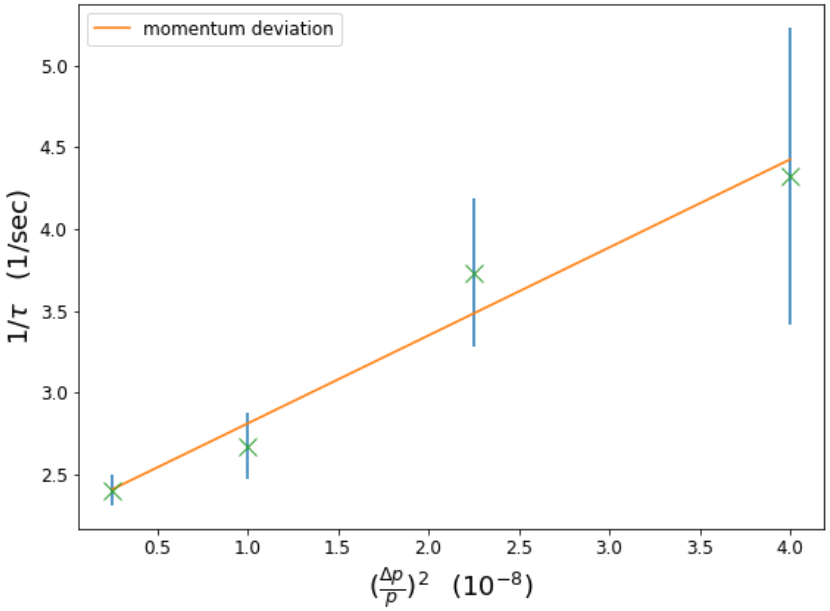

Figure 6.7.: The relationship between the square of the momentum spreads and the reciprocal of SCTs. The x-axis is the square of the momentum spread-sandand the y-axis is the inverse of SCTs. The orange line is the applied linear fit.

6.3. Chromaticity scan

Spin tune spread leads to a shorter SCT. The main contribution is the average path length change due to betatron and synchrotron motions as well as intrinsic resonances. The three groups of sextupole (MXS, MXL and MXG) in COSY (see Figure 5.2) are located at the large places of β_x, β_y and dispersion in the arc parts, respectively. In order to find the possible chromaticity (ξ_x, ξ_y) values, a 3D scan routine for adjusting the sextupoles settings is used.

6.3.1. Sextupole and chromaticity

According to the previous theory discussions, the additional quadrupole strength generated by the sextupole is:

$$k_{sext} = mx = mD\frac{\Delta p}{p} \tag{6.1}$$

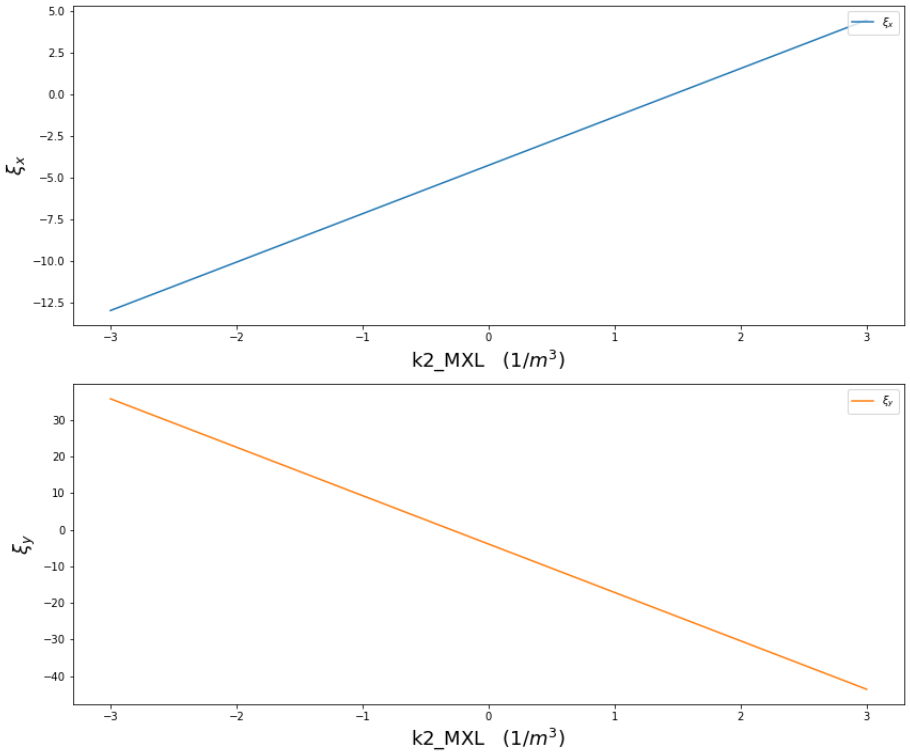

Figure 6.8.: Horizontal (top) chromaticity or vertical (bottom) chromaticity as a function of the normalized MXL sextupoles strength. The scan range of k_2 is (-3, +3) $[1/m^3]$.

where m is the sextupole strength, D is the dispersion and $\Delta p/p$ is the momentum spread. In Bmad, the normalized sextupole strength k_2 is more commonly used. It is defined as:

$$k_2 = \frac{q}{p}m, \tag{6.2}$$

with q being the particle charge and p the momentum.

One can use the scanning routine to benchmark the effect of each family's sextupole on the chromaticity. When the sextupole of one family was being checked, the sextupoles of other families were set to zero. The range of the normalized sextupole strength k_2 is (-3, +3) $[1/m^3]$.

The scanning results are illustrated in the graphs below. Figure 6.8 shows the chromaticity in the horizontal and vertical directions respectively as a function of the normalized strength of MXL sextupoles. For MXS and MXG families, see Figure A.1 in Appendix A. It can be seen that the sextupole strength is strictly linear with respect to the chromaticities in both directions. Among them, since the MXG sextupoles are located where the dispersion is the largest, the MXG family has the greatest effect on chromaticity. All the results are consistent with theory.

6.3.2. Zero chromaticities

Considering the path length change due to betatron motions, the chromaticities (ξ_x, ξ_y) in Equation 4.26 should be zero. In order to find the possible zero chromaticities, a 3D scan routine for adjusting the sextupoles settings is used.
After two iterations the optimal settings can be found. First do a rough scan with ($121 \times 101 \times 101$) grids to locate approximate ranges. One can find that (ξ_x, ξ_y) $\approx (0, 0)$ points are nearly at a fixed MXL setting. Then the second iteration uses these ranges to perform a finer scan with ($121 \times 101 \times 401$) grids. The resulting sextupole settings and optical parameters are listed in Table 6.4. Since only the sextupoles have been changed, the betatron tunes remain the same. Based on these settings, one can perform a spin tracking simulation, and the obtained spin coherence time was plotted in the Figure 6.9. The SCT is only $0.192 \pm 0.016\,s$, obviously, such a short SCT cannot meet our experimental requirements.

k2_mxl	k2_mxg	k2_mxs	Q_x	Q_y	ξ_x	ξ_y
-0.5365	+1.4835	-2.9260	+3.6322	+3.7182	+0.0002	-0.0002

Table 6.4.: The sextupoles setting and optical parameters obtained from the scan. $k2$ are the normalized strength of three families (MXL, MXG and MXS) sextupoles, Q_x and Q_y are the betatron tune in the horizontal and vertical planes respectively, ξ_x and ξ_y are the chromaticity in the horizontal and vertical planes respectively.

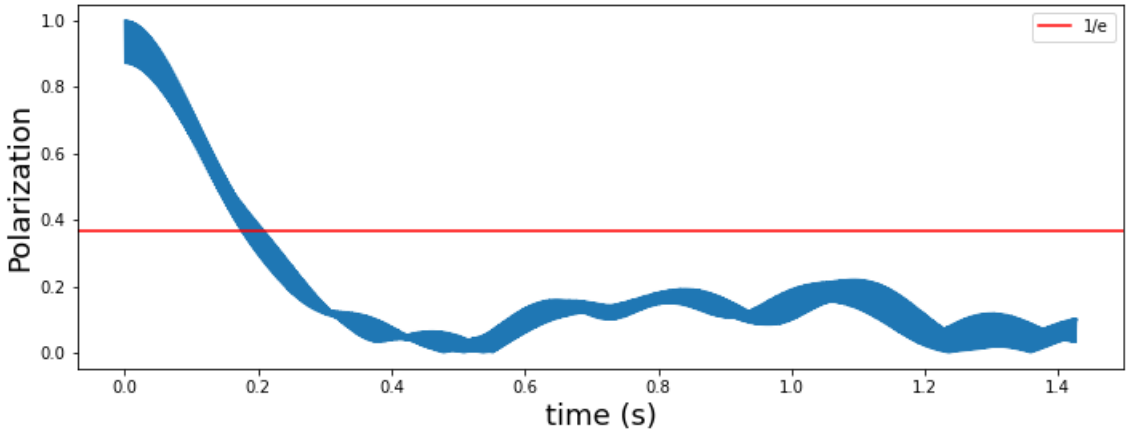

Figure 6.9.: Spin coherence time for a polarized proton beam with zero chromaticity (ξ_x, ξ_y) = (0, 0). The x-axis is the time and the y-axis is the total polarization. A red line indicates that the total polarization drops to 1/e of the initial polarization, and the corresponding time is the spin coherence time.

Next one can investigate some integer chromaticity points around the $(\xi_x, \xi_y) = (0, 0)$ point by using the same method. The results of scanning, spin tracking simulations as well as second-order momentum compaction factor α_1 are shown in the following Table 6.5. To reduce the effect of emittances on the results, one can also use another beam with smaller emittances to do the spin tracking. It can be seen that zero chromaticity is not the point where the SCT is maximum.

Table 6.5.: Spin coherence time of some integer chromaticity points. The first column is the chromaticity of horizontal and vertical planes, while the second column is the second-order momentum compaction factor α_1. The third column is the SCT when emittances are set to $\varepsilon_x = \varepsilon_y = 0.5\,mm\,mrad$ and in the fourth column is the SCT when emittances are set to $\varepsilon_x = \varepsilon_y = 0.1\,mm\,mrad$.

(ξ_x, ξ_y)	α_1	$SCT_{0.5}$ (sec)	$SCT_{0.1}$ (sec)
(0, 0)	-6.28	0.192 ± 0.016	0.544 ± 0.044
(0, -1)	-3.89	0.225 ± 0.017	0.713 ± 0.023
(-1, 0)	-2.63	0.222 ± 0.011	0.810 ± 0.027
(1, 0)	0.30	0.190 ± 0.019	0.800 ± 0.062
(0, 1)	1.23	0.180 ± 0.014	0.763 ± 0.030

6.3.3. Searching for minimal spin tune spread

In this section, the minimum spin tune spread $\Delta\nu_s$ was found using the scanning method. First the chromaticity of a working point is determined using the scanning program, then three beams with deviations are used for the spin tracking simulations, and finally the tracking results are analysed to obtain $\Delta\nu_s$. The three beams used in the simulation have deviations in the horizontal direction, vertical and longitudinal directions respectively.

The experience from the previous scan of $(\xi_x, \xi_y) = (0, 0)$ point shows that the value of MXL is fixed for a particular chromaticity. So one can start by scanning only the MXL sextupoles, keeping the other families of sextupoles at zero. Figure 6.10 illustrates the result of a 1-dimensional scan after two iterations. In the vicinity of the minimal $\Delta\nu_s$, one can fit a parabola to determine the minimum value of $\Delta\nu_s$.
Once the optimal MXL has been obtained, a 2-dimensional scan of the MXS and MXG is then performed. After tracking for 2000 turns at each point, the calculated $\Delta\nu_s$ are plotted in the Figure 6.11. After several iterations over the light-coloured (smaller $\Delta\nu_s$) region, the point with the minimum $\Delta\nu_s$ is obtained. Thus, the spin tune spread $\Delta\nu_s$ can be reduced by 3 orders of magnitude.
The results of the simulations obtained from the scans are listed in Table 6.6. Note that the point with the smallest $\Delta\nu_s$ does not overlap with the $(\xi_x, \xi_y) = (0, 0)$ point. Comparing the scan of the beam with momentum deviation to the beam with only x and y offsets shows that the chromaticities are very close between the two scans, while the α_1 of the former is closer to 0. The SCT has also increased significantly to

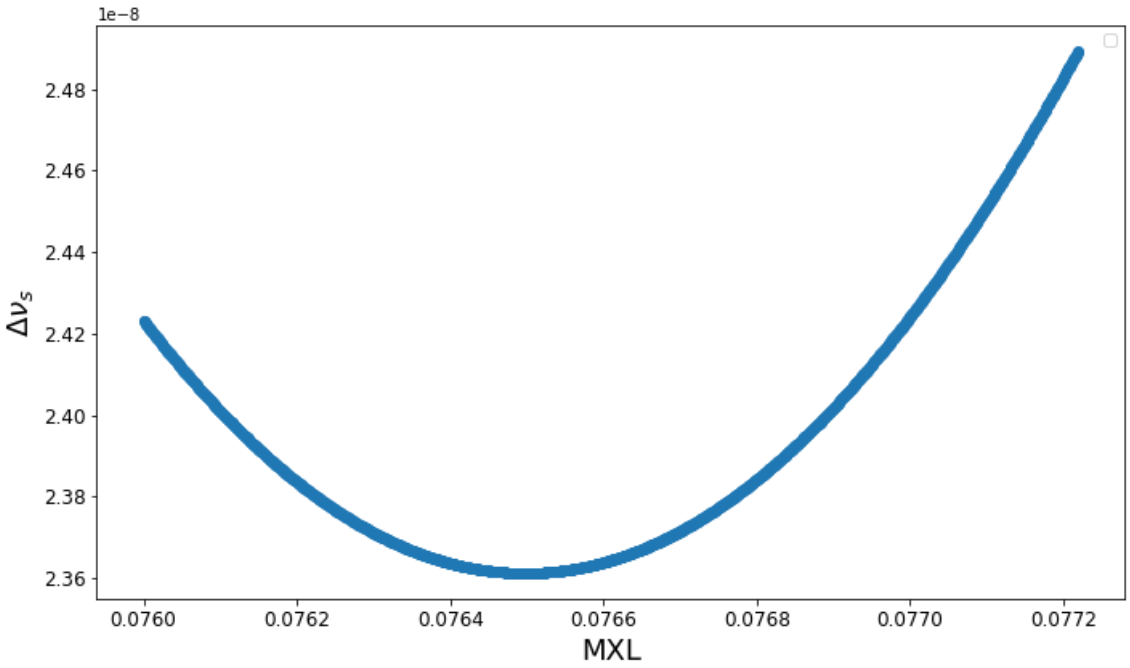

Figure 6.10.: Spin tune spread $\Delta\nu_s$ as a function of the normalized MXL sextupoles strength. The results are obtained after two iterations of 1-dimensional scanning.

	α_1	ξ_x	ξ_y	SCT(s)
$(\xi_x, \xi_y) = (0, 0)$	-6.284	+0.0002	-0.0002	0.192 ± 0.016
BMAD - Scan (x, y)	0.051	-3.9770	-4.9849	3.388 ± 0.151
BMAD - Scan (x, y, p)	0.005	-3.8676	-5.2498	7.009 ± 0.352

Table 6.6.: Spin tracking results of minimal spin tune spread via scan method. The first row is for point $(\xi_x, \xi_y) = (0, 0)$, the second row is the result of scanning the beams only with x and y offsets, and the third row is for the beams with additional momentum deviations. The columns in the table respectively show the second-order momentum compaction factor α_1, the chromaticity in the x and y directions and the SCT.

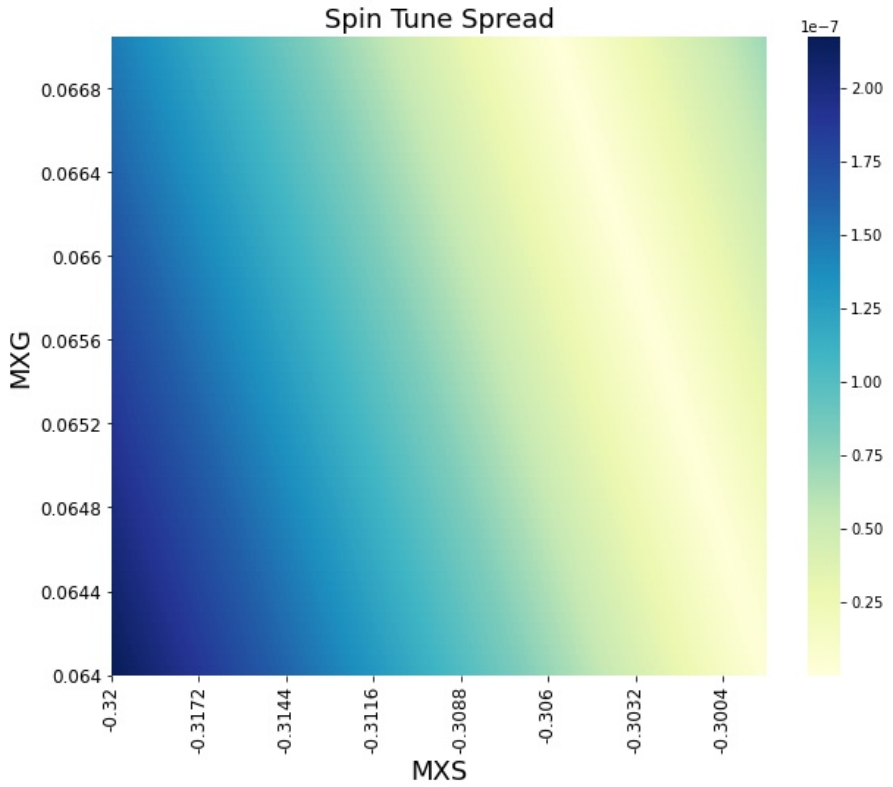

Figure 6.11.: The Spin tune spread $\Delta\nu_s$ is obtained after 2-dimensional scannings. Its value is accompanied by a colour, the larger the spin tune spread, the darker the colour. MXS and MXG are respectively the normalized strength of two families sextupole.

7.009 s, but there is still a long way to reach the expected value of 1000 s. In Figure 6.12, the SCT obtained after these two scans are shown respectively.

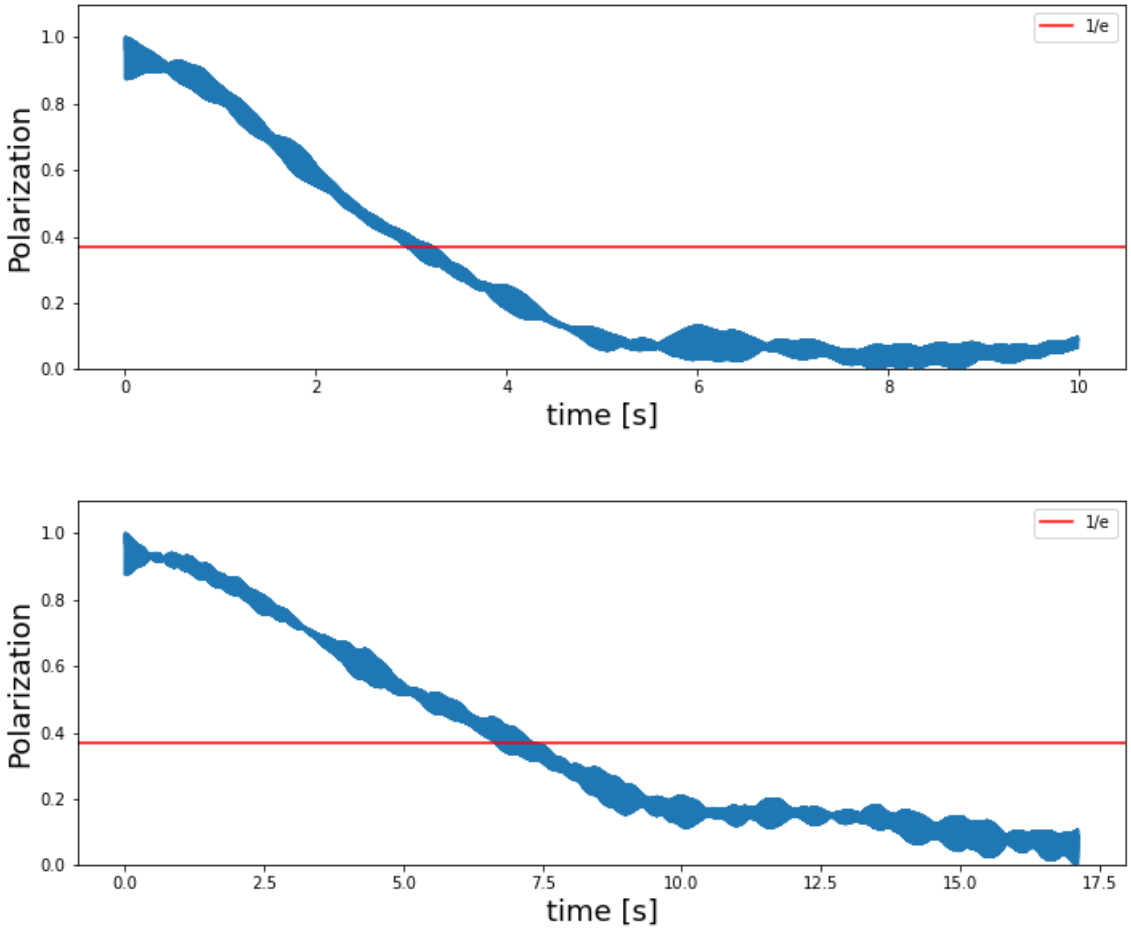

Figure 6.12.: Spin coherence time for a polarized proton beam with horizontal offsets and vertical offsets (top), plus additional momentum deviations (bottom). The x-axis is the time and the y-axis is the total polarization. A red line indicates that the total polarization drops to 1/e of the initial polarization, and the corresponding time is the spin coherence time.

7. Optimization of spin coherence time

7.1. Optimization method

In previous deuteron experiments, G. Guidoboni et al. suggested that the reciprocal of the SCT has a relationship with the sextupole magnet currents as follows:[22, 26]

$$\begin{aligned}\frac{1}{\tau} &= |A + a_1 I_s + a_2 I_L + a_3 I_G| \cdot \langle (\Delta x)^2 \rangle \\ &+ |B + b_1 I_s + b_2 I_L + b_3 I_G| \cdot \langle (\Delta y)^2 \rangle + O\langle (\frac{\Delta p}{p_0})^2 \rangle\end{aligned} \tag{7.1}$$

Here, τ is the SCT. Δx and Δy are the deviations of the particle in the x and y directions, which are the contributions of the horizontal and vertical emittance. A and B are the natural chromaticity, which is the chromaticity without the correction of the sextupole magnets. I_s, I_L and I_G are the currents applied to each of the three families of sextupoles. The subscripts S, L and G refer to the corresponding families of sextupoles in the arc section (MXS, MXL and MXG). a_i and b_i are the coefficients of the currents.

Assuming that for the momentum deviation term, its coefficient also follows a similar linear relationship.[36] Since the spin tune spread is proportional to $1/\tau$, one can write the further step as:[20]

$$\begin{aligned}\frac{1}{\tau} &= |A + a_1 I_s + a_2 I_L + a_3 I_G| \cdot \langle (\Delta x)^2 \rangle \\ &+ |B + b_1 I_s + b_2 I_L + b_3 I_G| \cdot \langle (\Delta y)^2 \rangle \\ &+ |C + c_1 I_s + c_2 I_L + c_3 I_G| \cdot (\frac{\Delta p}{p_0})^2\end{aligned} \tag{7.2}$$

For a single particle with horizontal or vertical offsets or momentum spread, one can change the settings of one family sextupoles (e.g. MXG), while all other families of sextupoles are set to zero. By using the FFT/NAFF algorithm one can easily remove the modulation effects of synchrotron oscillations and obtain very precise spin tune values. The spin tune difference between a offset particle and the reference particle is calculated.
The results of proton beam's spin tune spread $\Delta\nu_s$ with momentum spread $\Delta p/p$ for MXG sextupole family is plotted in Figure 7.1, and for the MXL sextupole family with

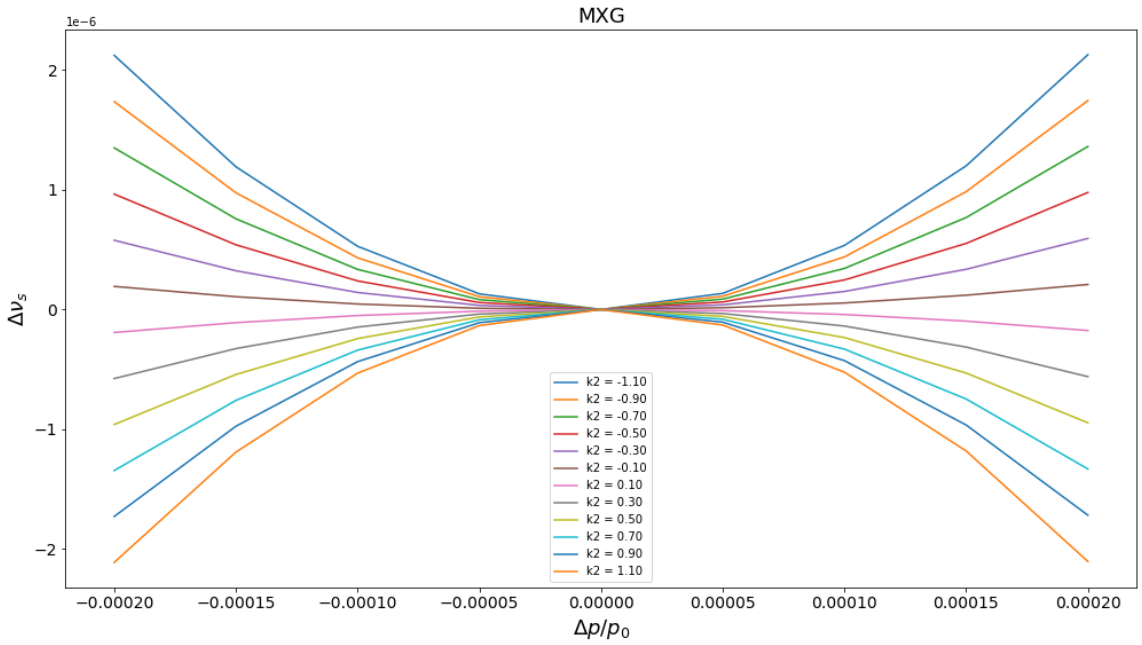

Figure 7.1.: Spin tune spread $\Delta\nu_s$ as a function of momentum spread $\Delta p/p$ for MXG sextupole family. Different normalized sextupole strengths $k2$ are shown in different colours, while the parabolas demonstrate clearly that they are all second-order curves.

horizontal or vertical offsets are shown in Figures B.1 in the Appendix B, respectively. The optimized settings for minimum $\Delta\nu_s$ can be obtained by flattening those resulting parabolas.

7.2. Linear equations approach

Our assumption is that the dependence of spin tune spread $\Delta\nu_s$ is linear for each family of COSY arc sextupoles. As there are three phase space coordinates to be optimised and three families of sextupoles located in the arc region available for variation, the following linear system of equations can be derived:[23]

$$\begin{aligned} \Delta\nu_{s,x} &= a_0 + a_1 I_s + a_2 I_L + a_3 I_G = 0 \\ \Delta\nu_{s,y} &= b_0 + b_1 I_s + b_2 I_L + b_3 I_G = 0 \\ \Delta\nu_{s,p} &= c_0 + c_1 I_s + c_2 I_L + c_3 I_G = 0. \end{aligned} \tag{7.3}$$

In order to minimise the spin tune spread $\Delta\nu_s$ in all phase space coordinates, the system of linear Equations 7.3 can be solved by the spin tracking simulations. This leads to an optimisation setup for the three sextupole families of COSY.
One can use a Bmad program to adjust one family sextupoles to the desired value, spin tracking simulations were performed for three separate beams with x, y and momentum offsets. Seven different values were chosen for each sextupole family, and the output data was analysed using a python script for linear fit. As an example of the sextupole family MXS, the Figures 7.2 and 7.3 show the results of the fits for the horizontal, vertical and longitudinal directions respectively.

The optimal normalized sextupole strengths obtained from the simulations are as follows:

$$\begin{aligned} k2\_mxs &= 0.09701016\ 1/m^3 \\ k2\_mxl &= 0.07542403\ 1/m^3 \\ k2\_mxg &= 0.00589589\ 1/m^3. \end{aligned}$$

Using these settings, one can find that spin tune spread was suppressed to -6×10^{-12}, which is the closest value to zero achieved so far. After a long 12 million turns spin tracking simulation (see Figure 7.4), the total polarization remains above 0.9. For the ideal COSY lattice, the optimal sextupole settings with the longest SCT of a proton beam was found.

	α_1	ξ_x	ξ_y	SCT(s)
BMAD - Scan (x, y, p)	0.005	-3.8676	-5.2498	7.009 ± 0.352
BMAD - Fitting Linear (x, y, p)	0.016	-3.7187	-5.1487	> 17

Table 7.1.: Spin tracking results of the optimization. The first row is for scanning the beams with momentum deviations, x and y offsets. The second row is the result of linear fitting method. Columns in the table refer to the second-order momentum compaction factor α_1, the chromaticity in the x and y directions and the SCT, respectively.

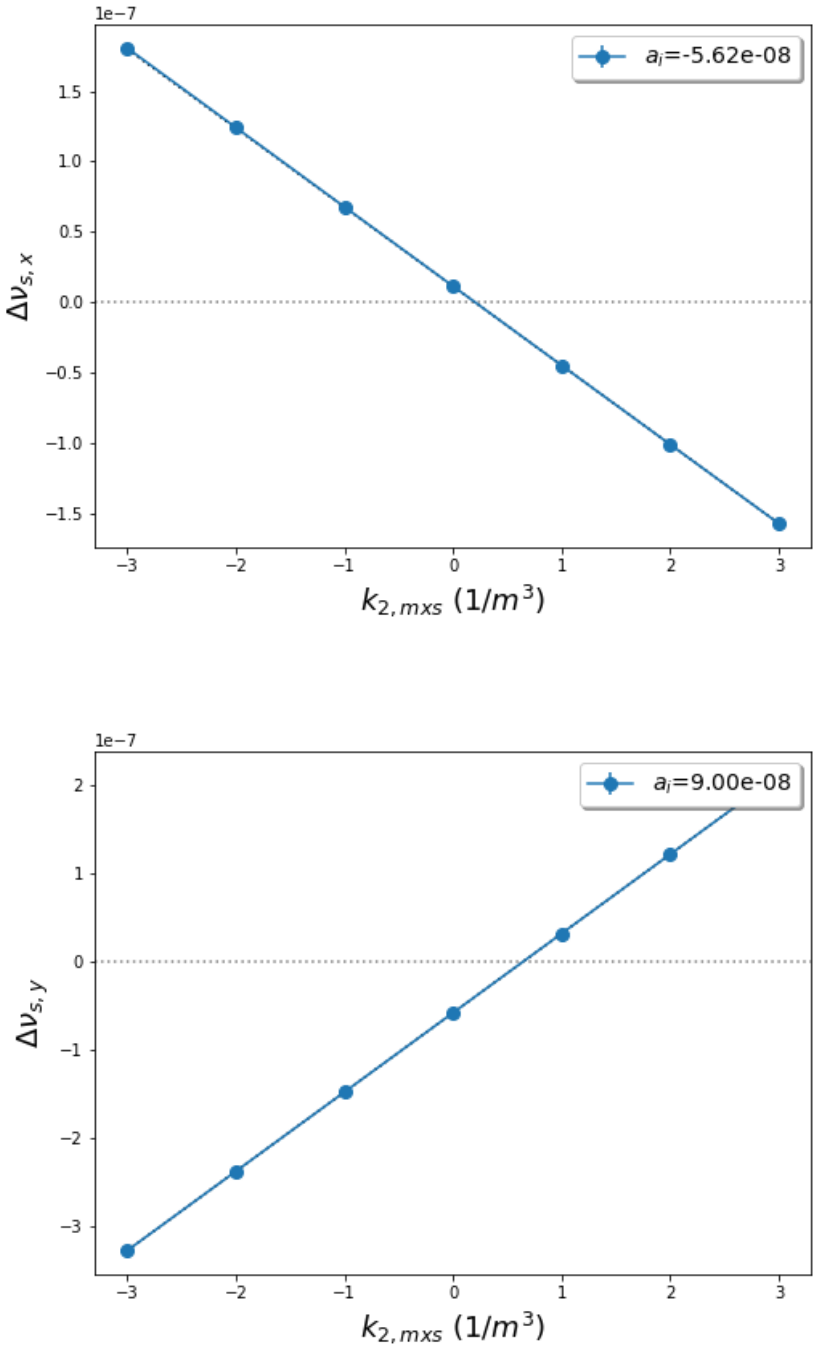

Figure 7.2.: Linear fittings in the horizontal (top) direction and vertical (bottom) direction. The blue dots represent the data from spin tracking simulations. The x-axis is the normalized MXS sextupole strength $k2$ and y-axis is the spin tune spread $\Delta\nu_s$. The fitted parameter a_i in the upper right of the plots refers to the coefficient a_1 of the MXS sextupole family current.

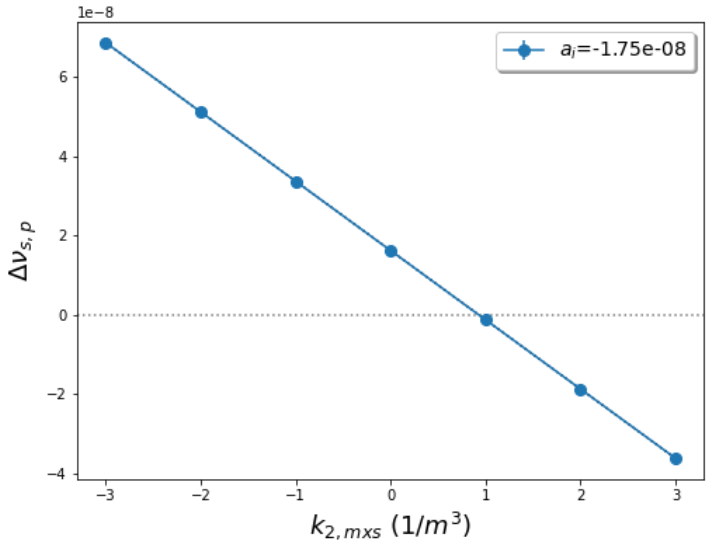

Figure 7.3.: A linear fitting in the longitudinal direction. The blue dots represent the data from spin tracking simulations. The x-axis is the normalized MXS sextupole strength $k2$ and y-axis is the spin tune spread $\Delta\nu_s$. The fitted parameter a_i in the upper right of the plots refers to the coefficient a_3 of the MXS sextupole family current.

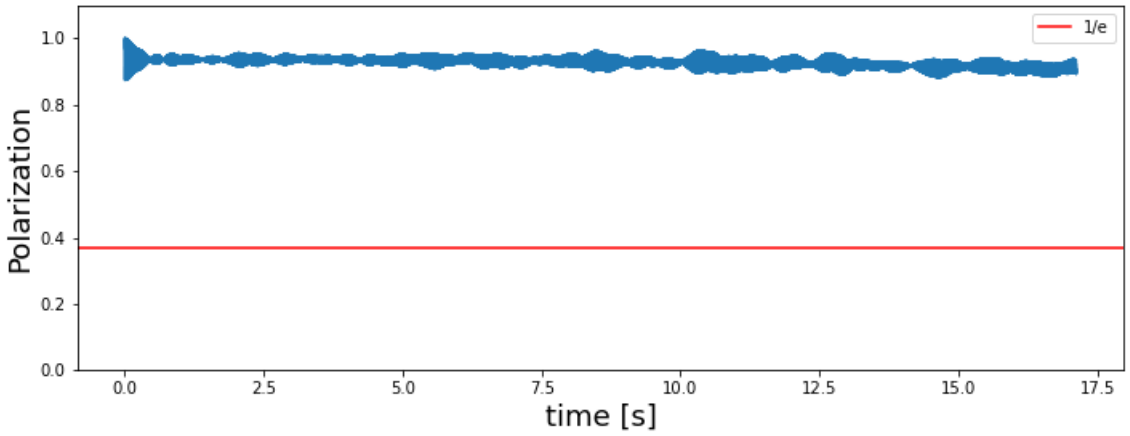

Figure 7.4.: Spin coherence time for a polarized proton beam with optimal sextupole settings. The x-axis is the time and the y-axis is the total polarization. A red line indicates that the total polarization drops to 1/e of the initial polarization, and the corresponding time is the spin coherence time.

In this chapter, a linear system of equations approach is used to optimise the three families of sextupoles located in the arc sections. The sextupole settings with zero spin tune spread were found by Bmad's simulations. The long SCT results were examined using spin tracking simulations.
The corresponding second-order momentum compaction factor α_1, horizontal and vertical chromaticity as well as the results obtained by the scanning method in the previous chapter are listed in Table 7.1.
The values of chromaticity are very close to those obtained earlier using the scanning method, both being negative. It is known that if all chromaticities are zero, there would be zero contribution from orbit lengthening caused by betatron motions. One possible reason for this is due to the ideal model used in this thesis. If the fringe fields of the magnet are also taken into account, the optimal sextupole settings will correspond to zero chromaticities.[34] This explanation still needs to be cross-checked by simulations using the Bmad program.
Furthermore, The difference between the two α_1 is very small and both are very close to 0. The contribution of α_1 is important for the SCT of proton beams. A delicate experiment design for measuring the α_1 is required.

8. Summary and outlook

The JEDI (Jülich Electric Dipole Moment Investigation) collaboration is pursuing the goal of measuring the Electric Dipole Moment (EDM) of protons with high precision for the first time at the Cooler Synchrotron COSY. Ensuring a long spin coherence time (SCT) is an important prerequisite for proton EDM measurements in storage rings. In this thesis, a COSY model without misalignments or field errors is implemented in the software library Bmad. After completing the benchmark, different algorithms for calculating the spin tune are discussed. A method based on fast Fourier transform (FFT) is presented which removes the modulation of synchrotron oscillations to obtain accurate results and saves a lot of computing time.

Based on the assumption that the particles follow the Gaussian distribution, the beam was generated for the spin tracking simulation. The results of the simulations after one million turns tracking show a negligible increase in the emittances of the beam, and the SCT of the beams produced by the 100 and 1000 particles are close to each other. Important parameters of the beam, such as emittances and the square of the momentum spread, were checked for their linear dependencies with the inverse of the SCT.
Besides, three families of sextupoles located in the arc section were varied to investigate the relationship between chromaticities and the SCT. Firstly, the SCT at zero chromaticity and nearby points were examined which revealed that the SCT was not at its maximum at $(\xi_x, \xi_y) = (0, 0)$. Subsequent searches were performed using a scanning program together with spin tracking simulations to try to find the point where spin tune spread $\Delta\nu_s$ is minimal. It was shown that only considering the chromaticity is not sufficient to achieve long SCT, the second order momentum compaction factor α_1 also plays an important role.

The observed second-order effects of Spin tune spread $\Delta\nu_s$ with emittances $(\varepsilon_x, \varepsilon_y)$ and the momentum deviation $\Delta p/p$, corresponding to different sextupole strengths, can be plotted as a family of parabolas. We assume that the coefficient of the square of the momentum deviation is also linear with the current strength applied to the sextupoles. Flattening these parabolas gives the optimal setting for the sextupoles. Solving the linear system of equations by simulation and fitting leads to a result that not only suppress $\Delta\nu_s$ to -6×10^{-12}, but also the SCT is much longer than before.

One possible explanation for why the chromaticity of the optimal SCT is not zero is due to the ideal model we used. Recent studies using different software have shown that the optimal point will coincide with the zero chromaticity point when

the fringe field is taken into account, which requires further simulations with Bmad to cross-check. In addition, the simulations show that the SCT is very sensitive to the beam parameters. This raises the requirement for a more accurate manipulation of chromaticity in future real experiments, and it is also very challenging to perform measurements for the second-order momentum compaction factor α_1.

Bibliography

[1] Llewellyn Hilleth Thomas. "I. The kinematics of an electron with an axis". In: *The London, Edinburgh, and Dublin Philosophical Magazine and Journal of Science* 3.13 (1927), pp. 1–22. URL: https://www.tandfonline.com/doi/abs/10.1080/14786440108564170.

[2] Valentine Bargmann, Louis Michel, and VL Telegdi. "Precession of the polarization of particles moving in a homogeneous electromagnetic field". In: *Physical Review Letters* 2.10 (1959), p. 435. URL: https://journals.aps.org/prl/abstract/10.1103/PhysRevLett.2.435.

[3] David Cohen. "Feasibility of Accelerating Polarized Protons with the Argonne ZGS". In: *Review of Scientific Instruments* 33.2 (1962), pp. 161–169. URL: https://aip.scitation.org/doi/abs/10.1063/1.1746524.

[4] ED Courant. *Acceleration of Polarized Protons to Relativistic Energies*. Tech. rep. Yale Univ., New Haven and Brookhaven National Lab., Upton, NY, 1962. URL: https://www.osti.gov/biblio/4718839.

[5] A. D. Sakharov. "Violation of CP Invariance, C asymmetry, and baryon asymmetry of the universe". In: *Pisma Zh. Eksp. Teor. Fiz.* 5 (1967), pp. 32–35. DOI: 10.1070/PU1991v034n05ABEH002497.

[6] Jacques Laskar. "The chaotic motion of the solar system: A numerical estimate of the size of the chaotic zones". In: *Icarus* 88.2 (1990), pp. 266–291. URL: https://www.sciencedirect.com/science/article/abs/pii/001910359090084M.

[7] R Bartolini et al. "Tune evaluation in simulations and experiments". In: *Part. Accel.* 52.CERN-SL-95-84-AP (1995), pp. 147–177. URL: https://cds.cern.ch/record/292773/files/sl-95-084.pdf.

[8] Shyh-Yuan Lee. *Spin dynamics and snakes in synchrotrons*. World Scientific Publishing Company, 1997. ISBN: 9789810228057.

[9] R. Maier. "Cooler synchrotron COSY — Performance and perspectives". In: *Nuclear Instruments and Methods in Physics Research Section A: Accelerators, Spectrometers, Detectors and Associated Equipment* 390.1 (1997), pp. 1–8. URL: https://www.sciencedirect.com/science/article/pii/S0168900297003240.

[10] D Prasuhn et al. "Electron and stochastic cooling at COSY". In: *Nuclear Instruments and Methods in Physics Research Section A: Accelerators, Spectrometers, Detectors and Associated Equipment* 441.1 (2000), pp. 167–174. URL: https://www.sciencedirect.com/science/article/pii/S0168900299011286.

[11] Klaus Wille. *The physics of particle accelerators: an introduction*. Clarendon Press, 2000. ISBN: 9780198505495.

[12] Werner Bernreuther. "CP violation and baryogenesis". In: *CP Violation in Particle, Nuclear and Astrophysics*. Springer, 2002, pp. 237–293. URL: https://arxiv.org/abs/hep-ph/0205279.

[13] FJM Farley et al. "New method of measuring electric dipole moments in storage rings". In: *Physical review letters* 93.5 (2004), p. 052001. URL: https://journals.aps.org/prl/abstract/10.1103/PhysRevLett.93.052001.

[14] Bernd Lorentz et al. "Status of the cooler synchrotron COSY-Juelich". In: *9th EPAC, Lucerne* 1246 (2004). URL: https://accelconf.web.cern.ch/e04/papers/tuplt043.pdf.

[15] Yoshihiko Shoji. "Dependence of average path length betatron motion in a storage ring". In: *Physical Review Special Topics-Accelerators and Beams* 8.9 (2005), p. 094001. URL: https://journals.aps.org/prab/abstract/10.1103/PhysRevSTAB.8.094001.

[16] H.P. Schieck. *Nuclear Physics with Polarized Particles*. Springer Berlin Heidelberg, 2011. ISBN: 9783642242250.

[17] A Lehrach. *Accelerator related issues for storage ring EDM searches: spin dynamics*. Tech. rep. Jülich Internal Report, 2012. URL: http://collaborations.fz-juelich.de/ikp/jedi/public_files/usual_event/EDM_Bonn-AL.pdf.

[18] Takeshi Fukuyama and Alexander J Silenko. "Derivation of generalized Thomas–Bargmann–Michel–Telegdi equation for a particle with electric dipole moment". In: *International Journal of Modern Physics A* 28.29 (2013), p. 1350147. URL: https://arxiv.org/pdf/1308.1580.pdf.

[19] Yu Senichev et al. "Spin tune decoherence effects in electro-and magnetostatic structures". In: *Momentum* 2 (2013), p. 11. URL: https://accelconf.web.cern.ch/IPAC2013/papers/wepea036.pdf.

[20] G Guidoboni. "Spin Coherence Time Lengthening of a Polarized Deuteron Beam Using Sextupole Fields". In: *Proc. 6th International Particle Accelerator Conference (IPAC15)*. 2015, pp. 4066–4069. URL: https://accelconf.web.cern.ch/ipac2015/papers/thpf146.pdf.

[21] Helmut Wiedemann. *Particle accelerator physics*. Springer Nature, 2015. ISBN: 9783319307596.

[22] G Guidoboni et al. "How to reach a thousand-second in-plane polarization lifetime with 0.97- GeV/c deuterons in a storage ring". In: *Physical review letters* 117.5 (2016), p. 054801. URL: http://collaborations.fz-juelich.de/ikp/jedi/public_files/colpapers/SCT_PhysRevLett.117.054801.pdf.

[23] Marcel Rosenthal. "Experimental benchmarking of spin tracking algorithms for electric dipole moment searches at the cooler synchrotron COSY". PhD thesis. Universitätsbibliothek der RWTH Aachen, 2016. URL: http://collaborations.fz-juelich.de/ikp/jedi/public_files/theses/Thesis_MRosenthal.pdf.

[24] A.A. Skawran. "Comparison of Frozen and Quasi Frozen Spin Concepts for a Deuteron Electrical Dipole Moment Storage Ring". MA thesis. Universitätsbibliothek der RWTH Aachen, 2016. URL: http://collaborations.fz-juelich.de/ikp/jedi/public_files/theses/Thesis-final.pdf.

[25] Nodoka Yamanaka and Emiko Hiyama. "Standard model contribution to the electric dipole moment of the deuteron, 3H, and 3He nuclei". In: *Journal of High Energy Physics* 2016.2 (2016), pp. 1–50. URL: https://link.springer.com/article/10.1007/JHEP02(2016)067.

[26] G Guidoboni et al. "Connection between zero chromaticity and long in-plane polarization lifetime in a magnetic storage ring". In: *Physical review accelerators and beams* 21.2 (2018), p. 024201. URL: https://journals.aps.org/prab/abstract/10.1103/PhysRevAccelBeams.21.024201.

[27] Jamal Slim. "A novel waveguide RF Wien filter for electric dipole moment measurements of deuterons and protons at the COoler SYnchrotron (COSY)/Jülich". PhD thesis. Universitätsbibliothek der RWTH Aachen, 2018. URL: https://publications.rwth-aachen.de/record/748558.

[28] Brian D Fields et al. "Big-bang nucleosynthesis after Planck". In: *Journal of Cosmology and Astroparticle Physics* 2020.03 (2020), p. 010. URL: https://arxiv.org/abs/1912.01132.

[29] H Schmickler. "Time-domain and Frequency-domain Signals and their Analysis". In: *arXiv preprint arXiv:2009.14544* (2020). URL: https://arxiv.org/abs/2009.14544.

[30] Wolfgang Hillert. "Transverse linear beam dynamics". In: *arXiv preprint arXiv:2107.02614* (2021). URL: https://arxiv.org/abs/2107.02614.

[31] Vera Poncza. "Extensive optimization of a simulation model for the electric dipole moment measurement at the Cooler Synchrotron COSY". PhD thesis. Universitätsbibliothek der RWTH Aachen, 2021. URL: http://collaborations.fz-juelich.de/ikp/jedi/public_files/theses/PhD_thesis_VPoncza_publish.pdf.

[32] Vera Poncza, Andreas Lehrach, et al. *Simulation Model Improvements at the Cooler Synchrotron COSY Using the LOCO Algorithm*. Tech. rep. JARA-FAME, 2021.

[33] Alexander Wu Chao. *Special Topics in Accelerator Physics*. World Scientific, 2022. ISBN: 9789811253492.

[34] Aleksei Melnikov. Private Communication. Forschungszentrum Jülich, 2022.

[35] D Sagan. *Bmad manual*. Tech. rep. Tech. rep., Cornell University, 2022. URL: https://www.classe.cornell.edu/bmad/manual.html.

[36] Maximilian Vitz. Private Communication. Forschungszentrum Jülich, 2022.

[37] *PyNAFF*. URL: https://pypi.org/project/PyNAFF/ (visited on Sept. 25, 2022).

Acknowledgement

First and foremost, I would like to express my deepest appreciation to my supervisor Prof. Dr. Andreas Lehrach. He offered a very fascinating lecture on accelerator physics and gave me the opportunity to work in the accelerator facility to write my master's thesis. He has always been patient in explaining to me many problems in accelerator physics and has provided all kinds of help.

I would like to thank Prof. Dr. Jörg Pretz for agreeing to be my second supervisor. I would also like to thank GSI Helmholtz Centre for Heavy Ion Research and Dr. Ralf Gebel for offering me a contract to work at Nuclear Physics Institute (IKP), Forschungszentrum Jülich.

Special thanks to Max Vitz for his supervision, helpful discussions and assistance. He was very patient in teaching me to use Bmad from scratch, especially during the epidemic, and was always there to provide useful advice and help with my work.

I also want to express my thanks to everyone in the JEDI collaboration for the fruitful discussions at the weekly meetings. In particular, I would like to thank my classmate Mariia Manerova for her help over the past year.

Thank you to my fellow students Qi Shao, Dr. Feng Gao, Yigong Luan, Ruijia Yang, who have enriched my life during my master studies.

Finally I would like to express my gratitude to my parents, my family members and my wife Mingyu Pan. Thank you for supporting me in my studies and research in Germany and for the endless encouragement I received.

Appendix

A. Chromaticity scan

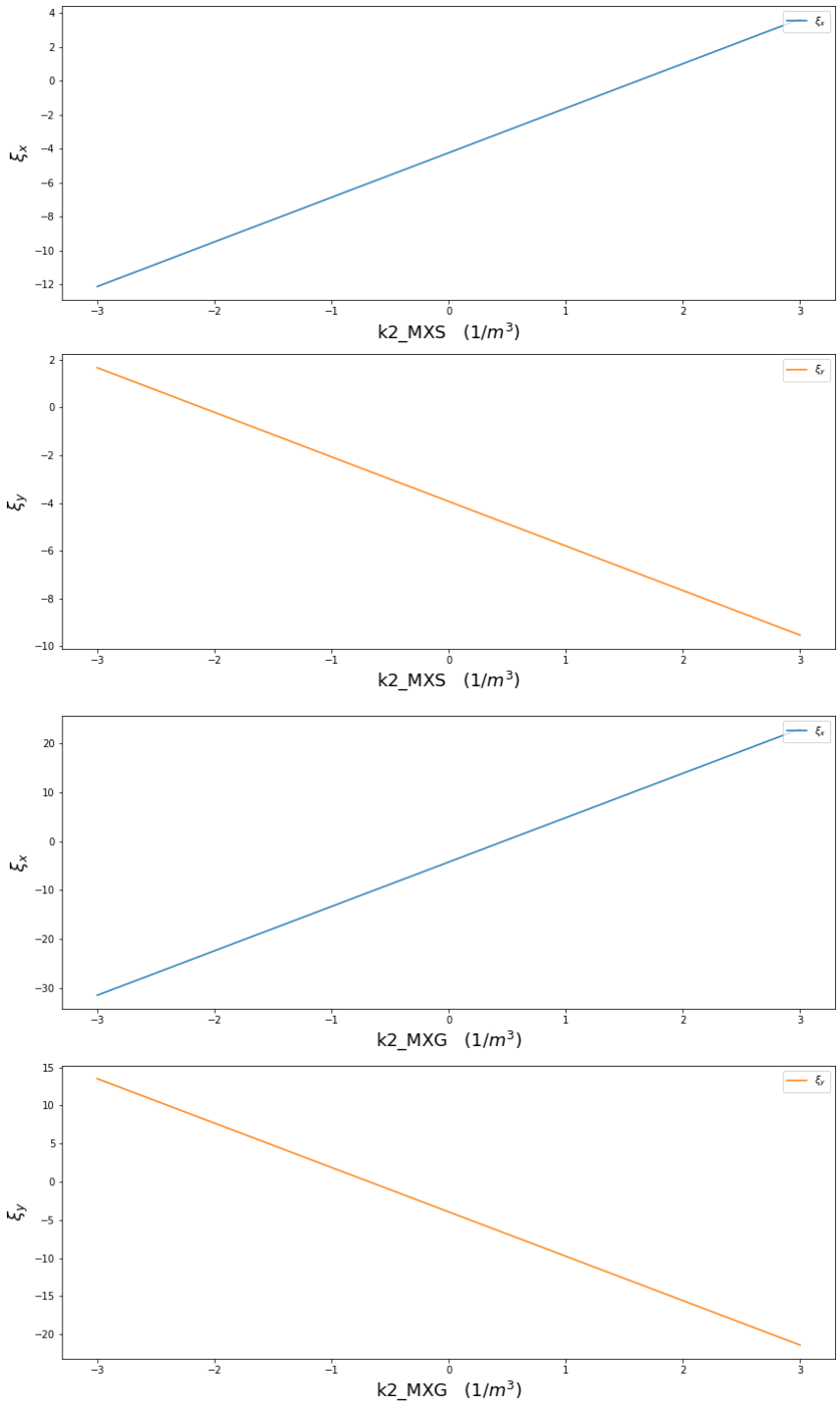

Figure A.1.: Horizontal (blue) chromaticity and vertical (yellow) chromaticity as a function of the normalized MXS (upper two graphs) and MXG (lower two graphs) sextupoles strength. The scan range of k_2 is (-3, +3) [$1/m^3$].

B. Optimization method

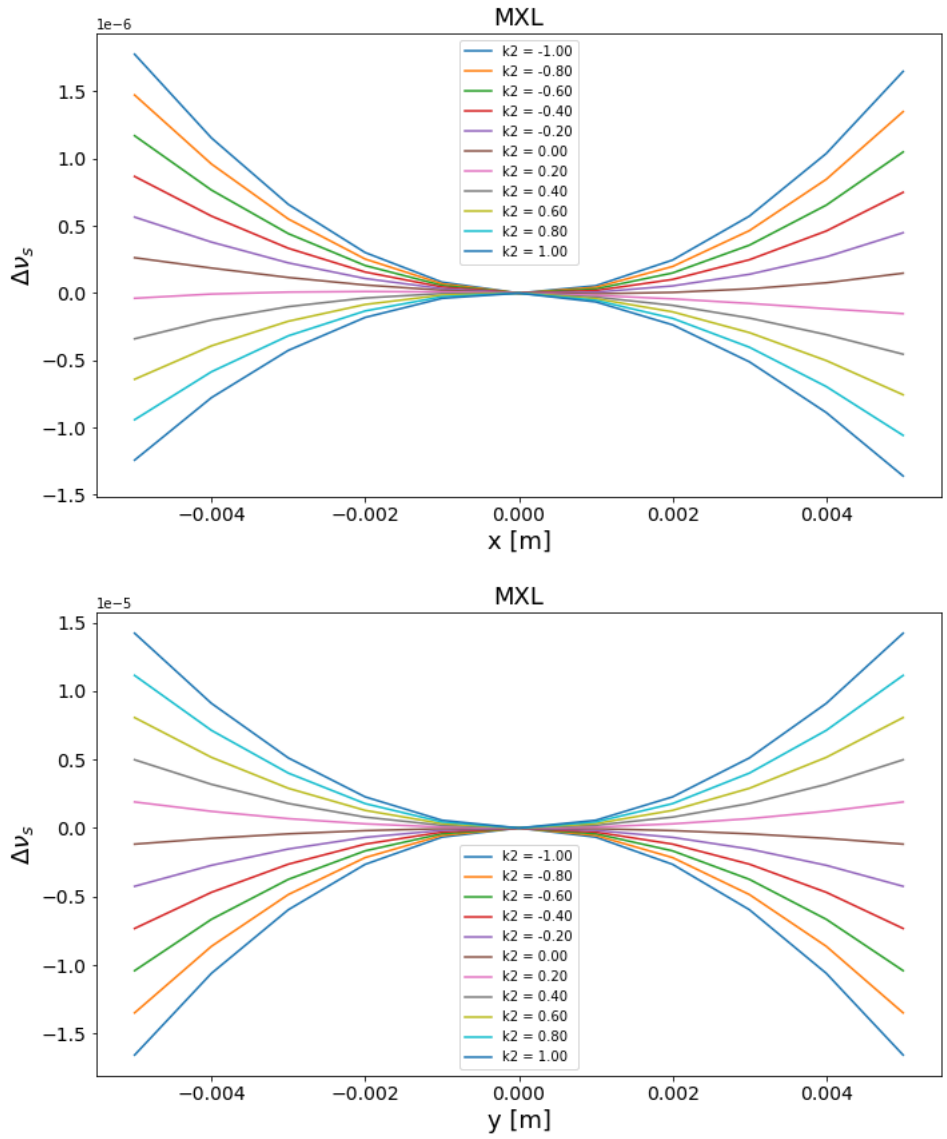

Figure B.1.: Spin tune spread $\Delta\nu_s$ as a function of horizontal offset x (top) or vertical offset y (bottom) for MXL sextupole family. Different normalized sextupole strengths $k2$ are shown in different colours, while the parabolas demonstrate clearly that they are all second-order curves.

Zentrales Prüfungsamt/Central Examination Office

Eidesstattliche Versicherung
Statutory Declaration in Lieu of an Oath

Gu, Daoning — Name, Vorname/Last Name, First Name

389735 — Matrikelnummer (freiwillige Angabe) / Matriculation No. (optional)

Ich versichere hiermit an Eides Statt, dass ich die vorliegende Arbeit/Bachelorarbeit/ Masterarbeit* mit dem Titel

I hereby declare in lieu of an oath that I have completed the present paper/Bachelor thesis/Master thesis* entitled

Investigation of the Spin Coherence Time for measuring the Electric Dipole Moment of Protons in the COSY Cooler Synchrotron

selbstständig und ohne unzulässige fremde Hilfe (insbes. akademisches Ghostwriting) erbracht habe. Ich habe keine anderen als die angegebenen Quellen und Hilfsmittel benutzt. Für den Fall, dass die Arbeit zusätzlich auf einem Datenträger eingereicht wird, erkläre ich, dass die schriftliche und die elektronische Form vollständig übereinstimmen. Die Arbeit hat in gleicher oder ähnlicher Form noch keiner Prüfungsbehörde vorgelegen.

independently and without illegitimate assistance from third parties (such as academic ghostwriters). I have used no other than the specified sources and aids. In case that the thesis is additionally submitted in an electronic format, I declare that the written and electronic versions are fully identical. The thesis has not been submitted to any examination body in this, or similar, form.

Aachen, 10.10.2022 — Ort, Datum/City, Date

Unterschrift/Signature

*Nichtzutreffendes bitte streichen

*Please delete as appropriate

Belehrung:
Official Notification:

§ 156 StGB: Falsche Versicherung an Eides Statt
Wer vor einer zur Abnahme einer Versicherung an Eides Statt zuständigen Behörde eine solche Versicherung falsch abgibt oder unter Berufung auf eine solche Versicherung falsch aussagt, wird mit Freiheitsstrafe bis zu drei Jahren oder mit Geldstrafe bestraft.

Para. 156 StGB (German Criminal Code): False Statutory Declarations
Whoever before a public authority competent to administer statutory declarations falsely makes such a declaration or falsely testifies while referring to such a declaration shall be liable to imprisonment not exceeding three years or a fine.

§ 161 StGB: Fahrlässiger Falscheid; fahrlässige falsche Versicherung an Eides Statt
(1) Wenn eine der in den §§ 154 bis 156 bezeichneten Handlungen aus Fahrlässigkeit begangen worden ist, so tritt Freiheitsstrafe bis zu einem Jahr oder Geldstrafe ein.
(2) Straflosigkeit tritt ein, wenn der Täter die falsche Angabe rechtzeitig berichtigt. Die Vorschriften des § 158 Abs. 2 und 3 gelten entsprechend.

Para. 161 StGB (German Criminal Code): False Statutory Declarations Due to Negligence
(1) If a person commits one of the offences listed in sections 154 through 156 negligently the penalty shall be imprisonment not exceeding one year or a fine.
(2) The offender shall be exempt from liability if he or she corrects their false testimony in time. The provisions of section 158 (2) and (3) shall apply accordingly.

Die vorstehende Belehrung habe ich zur Kenntnis genommen:
I have read and understood the above official notification:
Aachen, 10.10.2022

Ort, Datum/City, Date

Unterschrift/Signature